Summer 8-16-2024

Native Frequency Domain Monte Carlo Simulation of Spatial Frequency Domain Imaging for Look-Up Table Generation

Daemon A. Dikeman
University of Maine, daemon.dikeman@maine.edu

NATIVE FREQUENCY DOMAIN MONTE CARLO SIMULATION OF SPATIAL FREQUENCY

DOMAIN IMAGING FOR LOOK-UP TABLE GENERATION

By

Daemon A. Dikeman

B.S. Oregon State University, 2020

A THESIS

Submitted in Partial Fulfillment of the

Requirements for the Degree of

Master of Science

(in Biomedical Engineering)

Graduate School of Biomedical Engineering

The University of Maine

August 2024

Advisory Committee:

    Karissa Tilbury, Associate Professor of Biomedical Engineering, Advisor

    Michael Mason, Professor of Chemical & Biomedical Engineering

    Andre Khalil, Professor of Chemical & Biomedical Engineering

NATIVE FREQUENCY DOMAIN MONTE CARLO SIMULATION OF SPATIAL FREQUENCY DOMAIN IMAGING FOR LOOK-UP TABLE GENERATION

By Daemon A. Dikeman

Thesis Advisor: Karissa Tilbury

An Abstract of the Thesis Presented

In Partial Fulfillment of the Requirements for the

Degree of Master of Science

(in Biomedical Engineering)

August 2024

Early detection of diseases and injuries is critical for many treatments to be effective in achieving positive patient outcomes; this early detection is aided by accessible and non-invasive diagnostic methods including biophotonics. Tools such as Spatial Frequency Domain Imaging (SFDI) and Diffuse Optical Spectroscopic Imaging (DOSI) are two clinically relevant and powerful biophotonics techniques for identification and monitoring of disease and injury in medical settings, due to their utility in imaging and diagnosis, but recognizing their full potential necessitates advances in photon simulations to improve accuracy. The utility of SFDI in particular is heavily limited by the accuracy and applicability scope of available lookup tables (LUTs) generated by Monte Carlo simulations, with a disproportionate impact on marginalized communities due to unaddressed effects of varying levels of skin melanin. Monte Carlo Extreme (MCX) is a software suite which allows a fuller utilization of modern computing power through GPU acceleration for running simulations, improving processing speed by up to more than 100x compared to Monte Carlo Command Line, a software suite for running Monte Carlo simulations already commonly in use. The Gardner method is a method using Monte Carlo simulation for generating LUTs dependent on a mathematical transform; the Fourier method is a potentially novel method of using Monte Carlo simulations for generating LUTs described in this paper

which is more directly analogous to SFDI imaging processes which, we believe, could result in more accurate LUTs. In this work, MCX was utilized as a testbed to demonstrate the advantages and advances of the software with regard to rapid generation of LUTs and the potential of the Fourier method over the Gardner method. Specifically, we demonstrate the ability to spatially project patterns identical to those physically used in SFDI instrumentation. We benchmarked traditional Gardner-based Monte Carlo Simulation approaches in MCX as well as MCCL, comparing time requirements and accuracy of optical property determination for the Gardner method implemented in both software suites against an MCX Fourier illumination pattern approach. We found that MCX demonstrates speed improvements over MCCL ranging from 25x to upwards of 100x faster LUT generation speeds, and that the Fourier method showed marked advantages in accurate extraction of optical properties with a reduced rate of error compared to Gardner. The reduction of time required to generate various LUTs enables the ability to expand the range of LUTs to better encompass the role of melanin in various skin tones observed in clinical practice to improve accuracy of tissue chromophore extraction. Specifically, we found that failing to account for melanin concentrations associated with a broader range of skin-tones can result in upwards of 70% error in absorption coefficient extraction when using multi-layer LUTs with inaccurate skin optical property assumptions within the range of human skin tone variation. In summary, MCX-based Fourier-patterned photon simulations demonstrate promise in terms of reducing the computational burden of generating appropriate LUTs needed for implementing a broader and more accurate application of SFDI imaging in clinical practice.

UNIVERSITY OF MAINE GRADUATE SCHOOL LAND ACKNOWLEDGMENT

The University of Maine recognizes that it is located on Marsh Island in the homeland of Penobscot people, where issues of water and territorial rights, and encroachment upon sacred sites, are ongoing. Penobscot homeland is connected to the other Wabanaki Tribal Nations—the Passamaquoddy, Maliseet, and Micmac—through kinship, alliances, and diplomacy. The University also recognizes that the Penobscot Nation and the other Wabanaki Tribal Nations are distinct, sovereign, legal and political entities with their own powers of self-governance and self determination.

ACKNOWLEDGEMENTS

Thank you to my committee members for their patience and assistance, my family and friends for their support, and my wife for her endless encouragement and understanding.

TABLE OF CONTENTS

LIST OF TABLES

LIST OF FIGURES

LIST OF EQUATIONS

CHAPTER 1
INTRODUCTION & BACKGROUND

Spatial Frequency Domain Imaging (SFDI) is a non-invasive and low-cost imaging technique that images a wide area of tissue with healthcare applications including: 1) monitoring near-surface tissue oxygenation and capillary perfusion (Weinkauf, 2019), 2) monitoring pressure ulcer and diabetic necrosis risk factors (Yafi et al, 2017; Li et al, 2020), 3) monitoring wound or surgery recovery progress (Gioux et al, 2019; Draghici et al, 2018), 4) identification of near-surface tumors and proto-tumors (Tabassum et al, 2018), and 5) monitoring the severity of certain dermatologically relevant diseases (e.g. systemic sclerosis) (Pilvar et al, 2023).

SFDI fundamentally consists of the projection of light at different spatial frequencies, followed by processing, analysis, and comparison of the resulting diffuse reflectance (Gioux et al, 2019). As tissue is a low-pass filter, different spatial frequencies and wavelengths will produce different effective penetration depths. The diffuse reflectance emanating from the surface is dependent on both the optical scattering and absorption, collectively known as tissue optical properties (OPs) (Cuccia et al, 2009, Gioux et al, 2019). Judicious control of spatial frequency and wavelength enables the optical scattering and absorption properties to be separated analytically, with the optical absorption being used to quantify a variety of tissue chromophores, such as oxyhemoglobin and deoxyhemoglobin (Gioux et al, 2019).

To separate tissue optical properties from diffuse reflectance, forward models calculating the diffuse reflectance of varying optical scattering and absorption events for each spatial frequency are required. These forward models rely on either analytical approaches based on the radiative transport equation (RTE) and the diffusion approximation of light or numerical Monte Carlo simulations. As diffusion approximation relies on the assumption of an approximately 10:1 ratio of optical scattering to absorption, the diffusion approximation is not always applicable, particularly in tissues with low optical scattering, making solutions to the RTE exceptionally difficult to compute. Approaches reliant on Monte Carlo simulations may be limited

by available computational resources. However, recent software developments have enabled opportunities to directly match the instrumentation illumination patterns with Monte Carlo simulation models in addition to accelerating that modeling using graphical processing units (GPUs) for rapid, accurate generation of look-up tables (LUTs) - LUTs being reference tables used by functions to retrieve values based on certain input parameters - in SFDI, they are used to match detected diffuse reflectance to probable optical properties of the sample as a result of the difficulties of solving such problems analytically (see section 1.4 Modeling Photon Propagation).

In this document, we will first explain the basis and background of SFDI, followed by the fundamentals of the software in use during this study. We will then describe the tests performed, why we performed them, and what the results indicate.

1.1 Fundamentals of SFDI
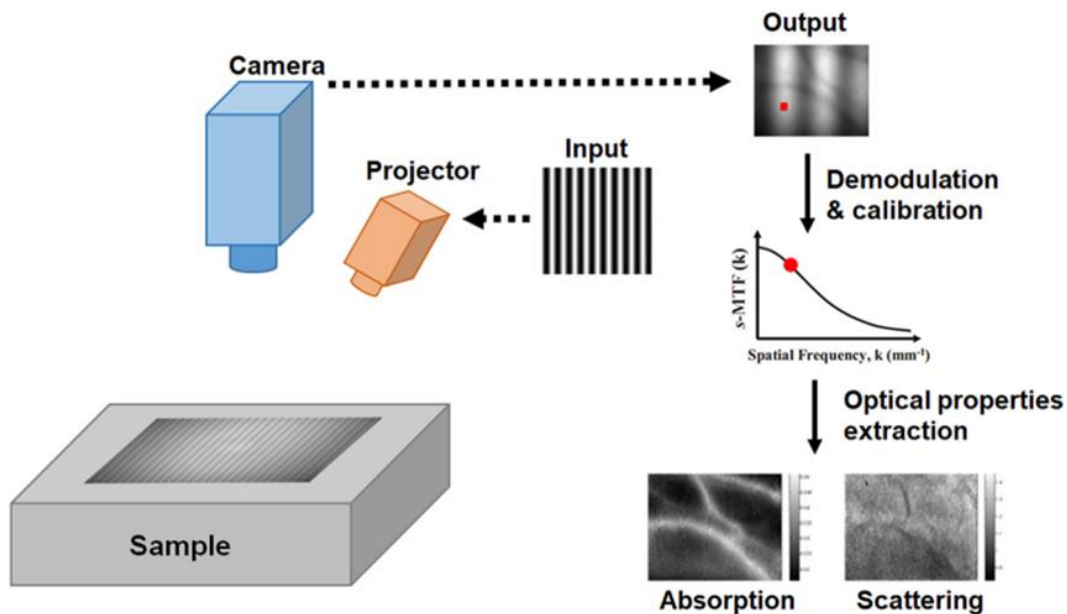
Figure 1: Diagram of SFDI process from Gioux et al, 2019

The process of SFDI (see Fig. 1) begins by choosing a set of spatial frequencies and an appropriate wavelength of light. Two-dimensional sinusoidal patterns (for non-zero spatial frequencies) with defined amplitude and phase are projected onto the sample. Three images

with unique phase shifts (0, 120, 240º) of the 2D sinusoidal pattern are used at each spatial

frequency are captured. The phase images at each spatial frequency are demodulated to

provide the modulation transfer function (MTF) as a function of spatial frequency, the first step

towards separating tissue scattering and absorption.

The most common spatial frequency combination to use in SFDI is 0.1 mm^{-1}, a

sinusoidal intensity pattern (AC), and 0 mm^{-1}, an unpatterned light projection (DC) with no

spatial intensity change. Diffuse reflectance, the light emanating from the tissue or phantom (an

object designed to mimic human tissue properties), is then imaged using a camera at each

wavelength, spatial frequency, and phase.

Single-pixel demodulation
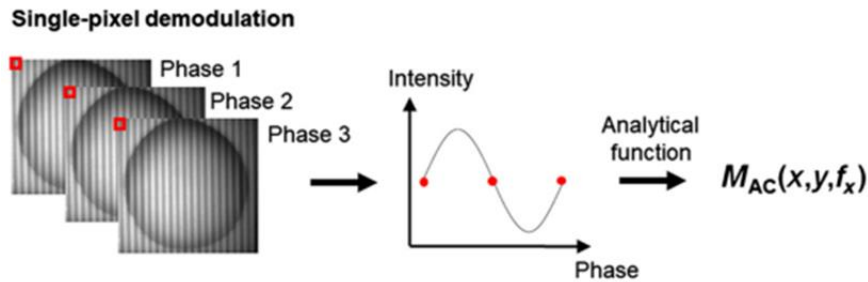
Figure 2: Single-pixel demodulation process flow diagram from Gioux et al, 2019.

Using the 3-phase images, the images are demodulated at every pixel (see Figure 2)

using the equation shown in Equation 1, for which $I^P(x,y)$ is the captured light intensity for the

pixel at the given x and y coordinates for a particular phase, with the subscript indicating the

phase shift from the standard in degrees, and $AC(x,y)$ is the resulting demodulated reflectance

value at the given x and y coordinates (Nadeau et al, 2014).

Equation 1.

$$AC(x,y) = \frac{\sqrt{2}}{3}\{[I_{0°}(x,y) - I_{120°}(x,y)]^2 + [I_{120°}(x,y) - I_{240°}(x,y)]^2 + [I_{240°}(x,y) - I_{0°}(x,y)]^2\}^{1/2}$$

The result of this demodulation is a single image for every wavelength and spatial

frequency tested. If the imaged surface is not flat, this image is subjected to surface correction

(measured via profilometry). SFDI requires the use of tissue phantoms during a calibration step

to account for the instrument response function and variability in the lighting conditions in the

testing environment. The resulting diffuse reflectance values enable extraction of optical property information by comparing the output from multiple distinct spatial frequencies at the same wavelength.

1.2 Light Tissue Interactions

Diffuse reflectance, or R_d, is a unitless measurement of the amount of light which returns to the camera after exiting the tissue relative to what was projected onto the tissue. Anisotropy, or g, is a measure of likely scattering direction; 0 is equally likely to scatter in any direction, while 1 is entirely forward (the same direction as the particle/photon was already traveling), and -1 is entirely backward (in the opposite direction as the particle/photon had been traveling). N is the index of refraction, while μ_s is the scattering coefficient and μ_a is the absorption coefficient - measures of how likely a photon is to scatter or be absorbed, respectively, per unit distance traveled within the medium. μ_s' is the reduced scattering coefficient, defined in Equation 2, and used to account for expected path divergence based on the anisotropy value.

Equation 2
$$\mu_s' = \mu_s * (1 - g)$$

In light propagation research, L^* is a unitless measure of expected path-length equal to the multiplicative inverse of the sum of μ_a and μ_s', as shown in Equation 3.

Equation 3
$$L* = 1 / (\mu_a + \mu_s')$$

R_d, μ_s, and μ_a are the most notable of these in SFDI modeling - the former being what is observed clinically in SFDI, and the latter two being used as the key components of LUT construction.

Table 1: Overview of Optical Properties

Optical Property	Abbreviation / Symbol	Brief Explanation	Typical Units
Diffuse Reflectance	R_d	Relative amount of returned light from a medium	None
Absorption Coefficient	μ_a	Rate of absorption per unit distance	mm^{-1}
Scattering Coefficient	μ_s	Scattering event rate per unit distance	mm^{-1}
Index of Refraction	n	Relative light wavelength reduction vs vacuum	None
Anisotropy	g	Metric of relative scattering direction probabilities	None
Reduced Scattering Coefficient	μ_s'	Anisotropy-adjusted scattering coefficient	mm^{-1}
Unitless Expected Pathlength	L^*	Unitless measure of anticipated typical path-length	None
Transport Mean Free Path	TMFP	Anticipated distance before net scattering behavior can be treated as entirely random.	mm

SFDI modeling consists of a forward model and an inverse model (see Fig. 3). The forward model is used to generate LUTs, running a simulation to test what diffuse reflectance results given a set of optical properties in simulated tissue in conjunction with a specified spatial frequency. The inverse model is used to fit the measured diffuse reflectance of the tissue or phantom and separate the optical scattering and absorption properties at the various spatial frequencies. To quantify the tissue optical properties, we use the linear interpolation function, griddata() in MATLAB and the inverse model to extract the optical properties (tissue scattering and absorption) from the measured diffuse reflectance, R_d.
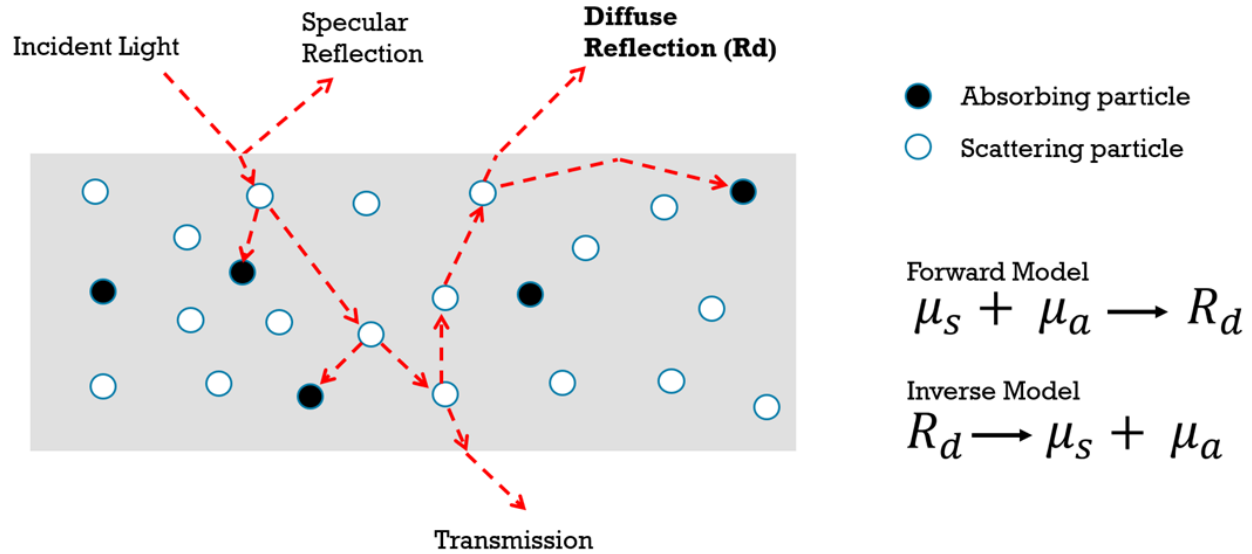
Figure 3: Representative diagram of photon interactions in tissue

Using the tissue absorption coefficient and Beer-Lambert law, the concentration of specific chromophores of interest (i.e. oxyhemoglobin or deoxyhemoglobin) can be quantified; see Equation 4, where A is attenuation, ε is molar absorptivity, l is length in centimeters, and c is concentration in mol/cm^3.

Equation 4 $A = \varepsilon l c$

However, as this form of the Beer-Lambert equation relies on a known path-length and does not account for attenuation due to losses from scattering, it cannot be used in isolation, as a basic linear model of path-length can only be used when the propagation regime is ballistic rather than random. Figure 4 demonstrates this behavior wherein photon propagation varies with scattering characteristics - as path length, scattering coefficient, and scattering anisotropy increase, the overall behavior of propagating photons in a medium will shift away from a standard ballistic regime and approach what is sometimes called a 'random walk'; however, this unpredictability only applies in the aggregate. The direction of any given photon under this behavioral regime continues to have the same characteristics as before, but the direction of any randomly selected photon from the set of photons subject to this behavioral regime will be impossible to predict based on the initial direction when projected into the tissue. In biological

tissues, the average distance between scattering events, the scattering mean free path, is typically around 100 µm, and the average distance before a randomly selected photon's direction will be effectively random, the transport mean free path, is around 1 mm (Busch et al, 1994).
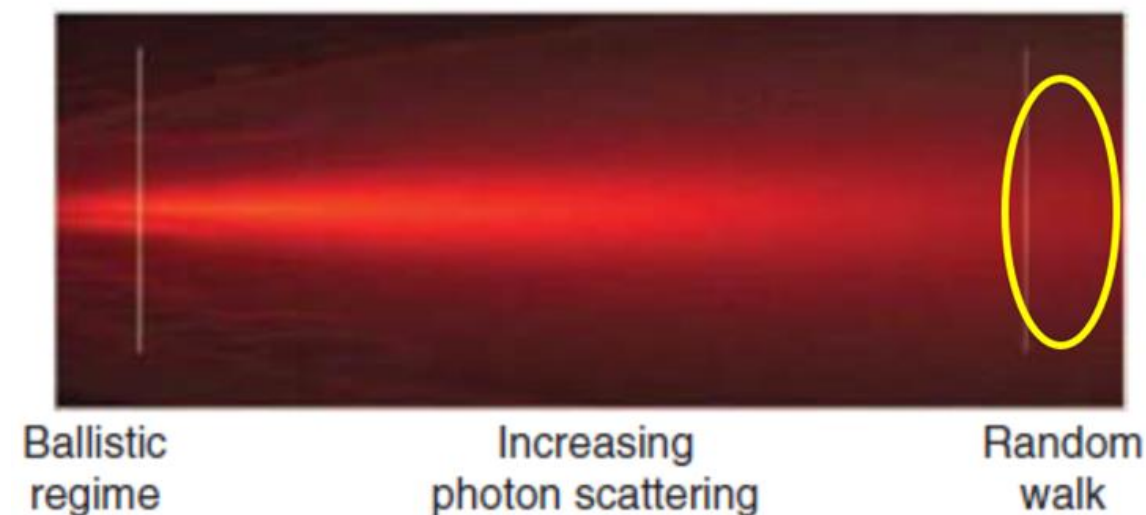
Fig. 4: Representative diagram of photon propagation characteristics with effective depth; base image from Ntziachristos, 2010.

SFDI's forward and inverse models together are able to resolve this, however: forward modeling generate look-up tables with combinations of optical properties which can then be used with the attenuated diffuse reflectance in the inverse model to generate absorption maps. These absorption maps can be used in conjunction with the Beer-Lambert Law and the extinction coefficient of the chromophores of interest for each wavelength to fit the concentration of chromophores (Cuccia et al, 2009).

1.3 Chromophore Extraction

The selection of light wavelength to project during imaging is crucial for determining chromophore concentration due to substance-dependent absorption spectrums. Excitation wavelength selection for optimal extraction of chromophores of interest within tissue is dependent on the number of chromophores of interest and their relationships to one another.

Isosbestic points, wavelengths at which the absorption of 2 or more chromophores are identical, are critically important for rigorous quantification of chromophore pairs (Nitzan 2014). For successful extraction of individual chromophores within a pair, the wavelength where the two chromophores have the highest relative differences in absorption must be identified. Ideally, this wavelength will be one where few other chromophores would have a significant impact on absorption. This extraction process uses the results at the selected isosbestic point to determine total concentration, and results at the wavelength of maximum difference to determine relative concentration of one of the paired chromophores. Contrasting this approach, solo chromophore extraction does not involve isosbestic points. As a result, accurate extraction is more dependent on the known optical properties of the background tissue and other nearby chromophores to select suitable wavelengths. The selected chromophores need to have sufficient contrast with other chromophores and background tissue to isolate the concentration of the chromophore of interest.

Two key chromophores of particular interest in SFDI are oxyhemoglobin and deoxyhemoglobin, which can provide crucial information on blood oxygenation levels. These two forms of hemoglobin share isosbestic points near 586nm and 808nm (see Figure 5), with ideal wavelength for an optimal signal to noise ratio for determining the concentration of these chromophores at 659nm (see Figure 5) At this wavelength, the relative absorption for deoxyhemoglobin is ten times greater than that of oxyhemoglobin (Meglinski & Matcher, 2002) and few other tissues have absorption coefficients as significant. However, melanin, a chromophore responsible for human skin pigmentation, also absorbs in this range. This complicates extraction and impairs accuracy when using oxy- and deoxyhemoglobin, as well as other tissue chromophores using this range.
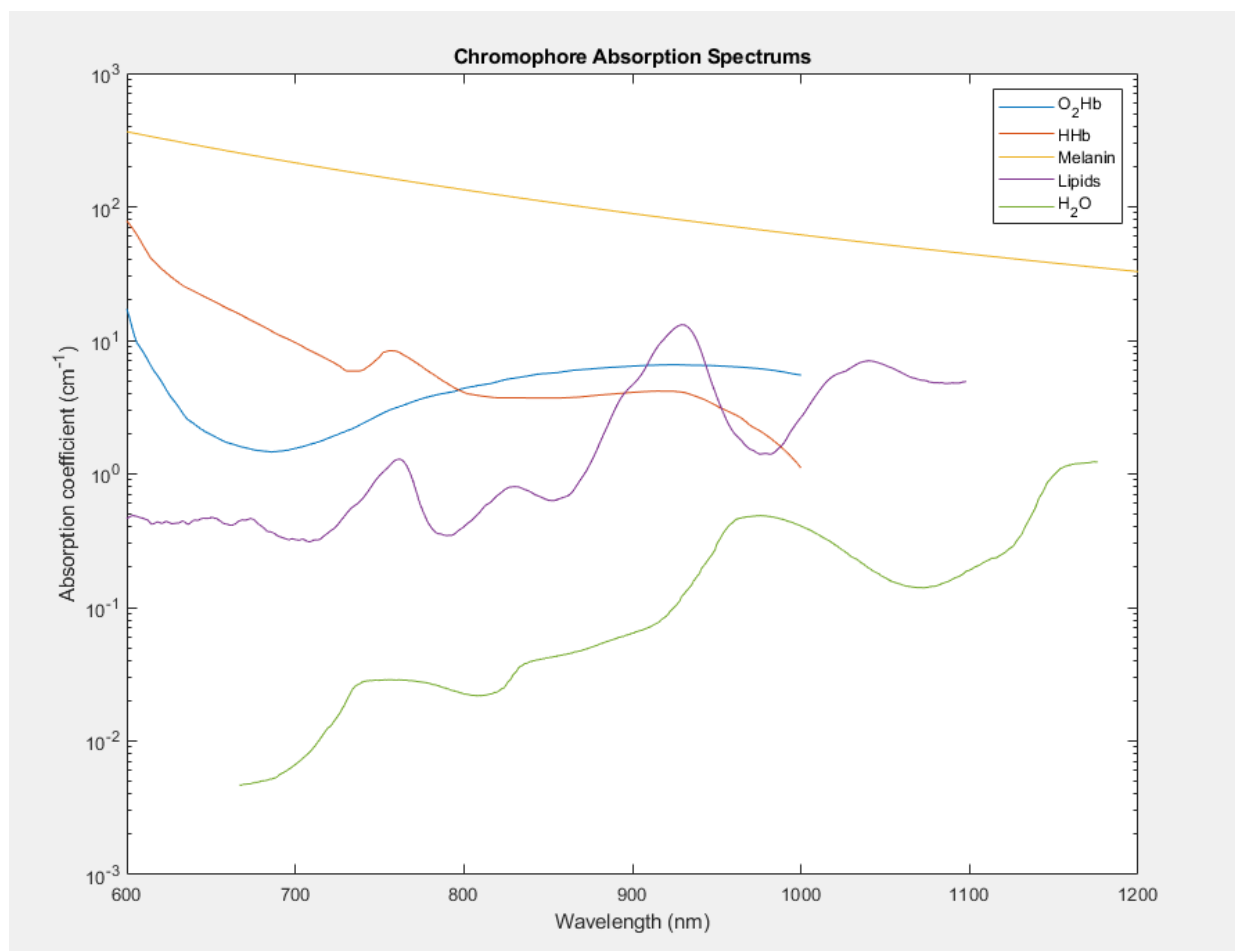
Fig 5: Absorption of most relevant chromophores of interest - oxyhemoglobin (O_2Hb),

deoxyhemoglobin (HHb), melanin, lipids and water (commonly anticipated secondary or

background chromophores). Data sourced from S. L. Jacques, 2018.

As melanin content varies widely (Meglinski & Matcher, 2002), utilizing an array of LUTs designed with the appropriate skin phenotypes in mind may be far more accurate than a generic LUT or applying LUTs built for a very different skin phenotype. Poorly fitted LUTs can result in poor outcomes for patients, as was seen during the COVID-19 pandemic, where non-Hispanic black patients were almost twice as likely to have hypoxemia that went undetected by pulse oximetry than their non-Hispanic white counterparts (Sudat et al, 2023; Sjoding et al, 2020; Bickler et al, 2005). To determine what LUT parameters are most appropriate, a patient's skin must be assessed objectively. Unfortunately, many of the historical skin tone classifications are

subjective, creating significant limitations in accurately extracting tissue chromophores from members of underrepresented populations. The Fitzpatrick scale, a classification schema for human skin tone developed in the 1970s to assist with psoralen and UVA (PUVA) therapy, (see Figure 6) has severely limited use for academic purposes, especially in contexts unrelated to sunburn as a result of its subjective, self-administered, and survey-based assessment methods (Phan et al, 2021). Placement on the Fitzpatrick scale is based on patients self-reporting their skin's reaction to sun exposure, on a spectrum from burning to tanning. Many other models have little to no scientific basis, such as von Luschan's chromatic scale, based purely on visual comparisons (Smith 2002).
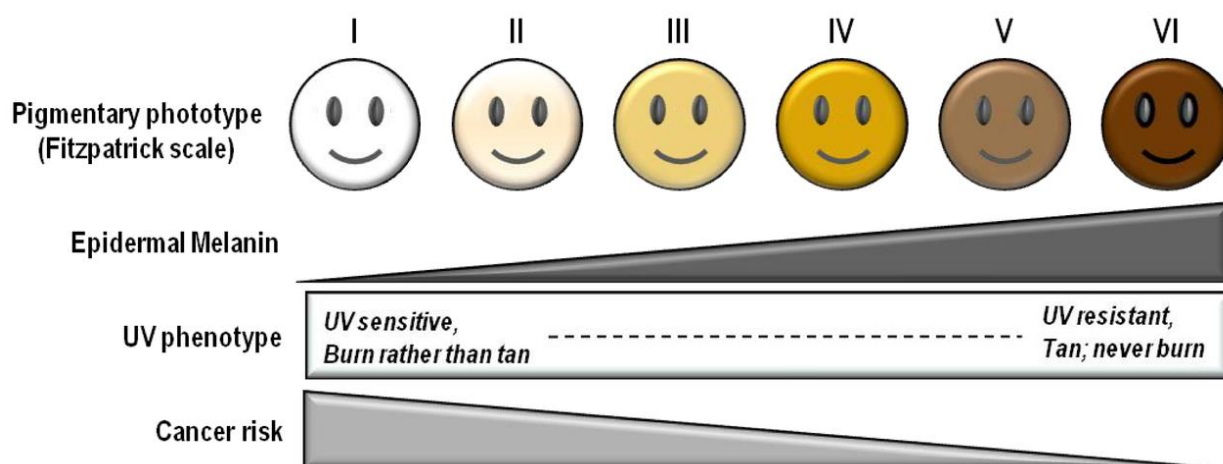
Fig 6: Fitzpatrick scale depiction of relative values showing six categorizations of skin and original purpose as basic skin cancer risk assessment tool.

Cutaneous colorimetry provides researchers with a more objective tool with which to assess skin color: the CIELAB color system, which represents color via three dimensions as seen in Figure 7: lightness (typically denoted by L* but marked as L** in this paper to avoid confusion with the L* parameter used in SFDI) which ranges from pure black at 0 to pure white at 100; a*, which indicates a red-green color component where +a* is more red and -a* is more green; and b*, which indicates a yellow-blue color component where +b* is more yellow and -b* is more blue.
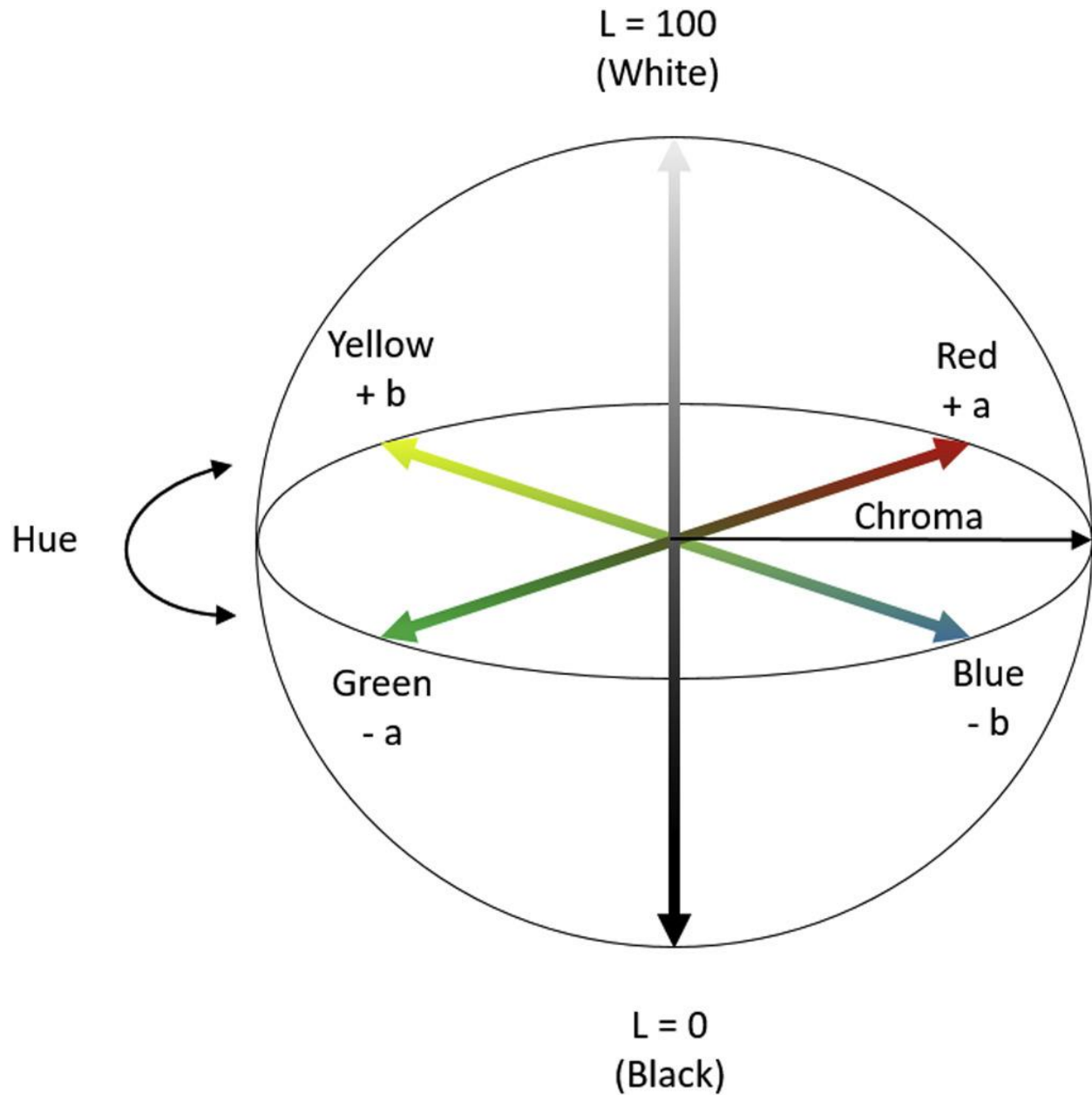
Figure 7: Representation of the triple axis color system used in cutaneous colorimetry.

These two chromaticity parameters align with the mechanisms of natural human vision in distinguishing and identifying color, and all three together are likely to present a very suitable mechanism for estimates of melanosome concentration, with L**, a*, and b* corresponding with total melanin, pheomelanin, and eumelanin concentration respectively. These estimates are limited however; human skin variation tends to range from L** values of 30 to 80 at the far extremes and increasing melanin concentration will eventually result in reduced chromaticity.

(Ly et al, 2020) Cutaneous colorimetry has been used in conjunction with SFDI to demonstrate a basic level of correlation between values in the CIELAB system and optical properties relevant to SFDI (Phan et al, 2022). Although this technique is very promising and a clear improvement over previous methods of skin tone assessment, the early state of current research makes apparent the necessity of additional research before melanosome concentration can be reliably estimated via colorimetry, which is beyond the scope of this project.

1.4 Modeling Photon Propagation

The radiative transfer equation (RTE) allows for the analytical modeling of energy transfer through a medium in the form of electromagnetic radiation based on absorption, emission, and scattering pattern. The RTE can be seen in Equation 5, where t is time, c is the speed of light in the tissue, μ_t is the extinction coefficient and equal to the sum of μ_s and μ_a (the scattering and absorption coefficients, respectively), P is a phase function representing the probability of light at angle s' scattering at the angle $d\Omega$ around direction s, and $S(r,s,t)$ represents the light source where r denotes position, s denotes direction, and t denotes time. Unfortunately, the RTE is very difficult to solve without approximations such as the diffusion approximation; these approximations result in the solution being computationally efficient, but limit the possible accuracy (Gardner & Venugopalan, 2011, Haskel et al, 1994).

Equation 5

$$\frac{\partial L(\vec{r}, \hat{s}, t)/c}{\partial t} = -\hat{s} \cdot \nabla L(\vec{r}, \hat{s}, t) - \mu_t L(\vec{r}, \hat{s}, t) + \mu_s \int_{4\pi} L(\vec{r}, \hat{s}', t) P(\hat{s}', \hat{s}) d\Omega' + S(\vec{r}, \hat{s}, t)$$

One common approximation for modeling photon propagation in biological tissues using the RTE is diffusion approximation, wherein it is assumed that optical scattering dominates at a ratio of at least 10:1 (Haskell et al, 1994). This assumption may be true for some light-skinned individuals, but becomes progressively less suitable for use as complexion darkens (Meglinski & Matcher, 2002; Bickler et al, 2005). Using the diffusion approximation, the RTE is reduced to the

diffusion equation, shown in Equation 6, where $\Phi(r,t)$ is the fluence rate and D is the diffusion coefficient of the medium.

Equation 6
$$\frac{1}{c}\frac{\partial \Phi(\vec{r},t)}{\partial t} + \mu_a\Phi(\vec{r},t) - \nabla \cdot [D\nabla\Phi(\vec{r},t)] = S(\vec{r},t)$$

The diffusion coefficient D is described in Equation 7, where μ_s' is the reduced scattering coefficient and μ_a is the absorption coefficient.

Equation 7
$$D = \frac{1}{3(\mu_a+\mu'_s)}$$

Another limitation of the diffusion approximation approach is the reliance upon an assumption of homogeneous tissue, neglecting the possibility of multiple layers with different properties (Alexandris et al, 1998). This assumption has been helpful in previous models for SFDI but suffers from inequitable patient care outcomes due to natural variations in human skin tone (Sudat et al, 2023). As melanin is only present in the epidermis, a layer of tissue commonly approximated as 100 microns thick (Meglinski & Matcher, 2002; Lister et al, 2012) simply modeling the change in skin tone as a change in a homogenous tissue layer is likely to result in errors as compared to a multilayer approach (Gardner & Venugopalan, 2011; Tabassum et al, 2018).

1.5 Numerical Simulation Approaches

The primary method of photon modeling for SFDI is currently Monte Carlo simulations. The Monte Carlo method of simulation uses large numbers of repeated random sampling trials and is very effective at modeling complex probabilistic systems which may be difficult to solve analytically. Equation 8 shows how to calculate diffuse reflectance, R_d, as a function of spatial frequency, f_x, with Monte Carlo simulations for SFDI, where N is the total number of photons simulated and W_n is the weight of the nth photon - the means of determining W_n being the primary differentiation between different Monte Carlo simulation methods (Gardner & Venugopalan, 2011).

Equation 8
$$R_d(f_x) = \frac{1}{N}\sum_{n=1}^{N} W_n$$

In the context of SFDI, several different options are available to perform these simulations with open-source tools - the foundational method being developed in stages by Steven Jacques and his graduate students between 1985 and 1999 (Jacques, 2022). Several software generations of improvements and advancements have been made since, most notably Monte Carlo Command Line (MCCL) developed by UC Irvine (Hayakawa et al, 2022), and more recently Monte Carlo Extreme (MCX) by Fang et al. (Fang & Boas, 2009).

CHAPTER 2

METHODS & SOFTWARE

2.1 Monte Carlo Command Line

Recently, MCCL has been the most commonly used software for generating LUTs, but suffers from requiring familiarity with shell interfaces that may present barriers to use. UC Irvine's Virtual Tissue Simulator (VTS), however, has a dedicated graphical user interface (GUI) which makes testing and interaction to understand certain basic functions involved in MCCL much easier. In our own research, we used the VTS for comparison testing regarding the behavior of R_d plots at varying values of L* and optical property ratios. A more significant limitation of MCCL is its reliance on the CPU for large numbers of similar calculations - a process more readily handled by the GPU in modern computing (Hayakawa et al, 2022).

2.1.1 Gardner Method Implementation

One method of Monte Carlo simulation readily implemented through MCCL is the Gardner method (Gardner & Venugopalan, 2011), which consists of a pencil beam illumination source projected normally onto the simulated tissue, with the resulting photon paths weighted based on the relevant spatial frequency and the resulting diffuse reflectance calculated via the following equation:

Equation 9
$$W_n = exp\left(-\mu_{a,1}d_{1,n} - \mu_{a,2}d_{2,n}\right) exp\left(-2\pi i f_x x_n\right)$$

Where $d_{i,n}$ is the total photon path length in the i'th layer, with subscripts 1 & 2 respectively indicating the top & bottom layers of a two-layer tissue model. The first term handles the effects of absorption, matching a conventional continuous absorption-weighted MC simulation, while the second term accounts for spatial modulation as a frequency-dependent phase accumulation; x_n is the net lateral displacement of photon exit location relative to source.

In practical terms, this means that the Gardner method is able to exploit the non-directionality of Beer-Lambert equation, using a pencil source and photon displacement-based weighting mechanism to simulate a distributed spatial frequency-based illumination for which

only the photons that end up in the origin point are considered. MCCL is able to make effective use of continuous calculations (Hayakawa et al, 2022), with arbitrary layer sizes and properties, and no requirement for an outer boundary on the simulated tissue area.

2.2 Monte Carlo Extreme

Recently, Dr. Qianqian Fang has developed Monte Carlo Extreme, or MCX, a GPU-based Monte Carlo simulation program which utilizes GPU acceleration to improve speeds by running many simultaneous computations of photon paths in parallel (Fang & Boas, 2009; Yan et al, 2020). The program is available in a number of forms for different applications, including Mesh-based Monte Carlo (MMC) which displays advantages when modeling complex tissue forms, MCX forOpenCL (MCX-CL) which is able to use a wider variety of GPUs and CPUs for processing, MCXStudio, an equivalent to VTS with a built-in GUI, and MCXLAB, which converts MCX's code into a MEX file able to called and managed directly from MATLAB. MCXLAB is the program used here due to the ease of adjustment, testing, and use thanks to MATLAB's convenient user interface and debugging tools (Fang & Boas, 2009). MCXLAB uses a voxel-based simulation to simplify photon path modeling calculations and tissue simulation, while diffuse reflectance can be captured by the use of detectors, a bounding box system, or a voxel-based pixel-like binning system for photon accumulation. The latter is directly comparable to the camera of actual SFDI instrumentation, and the option used for the simulations in this paper.

a) MCCL Virtual Simulator

Simulated Photons

Void/Air

Top layer(s)
(skin)

Bottom layer
(bulk tissue)

Void/Air

b)

MCX Voxel Simulation

Voxel Grid

c)

Skin Layer
Static Optical Properties

Bulk Tissue Layer
Varying Optical Properties
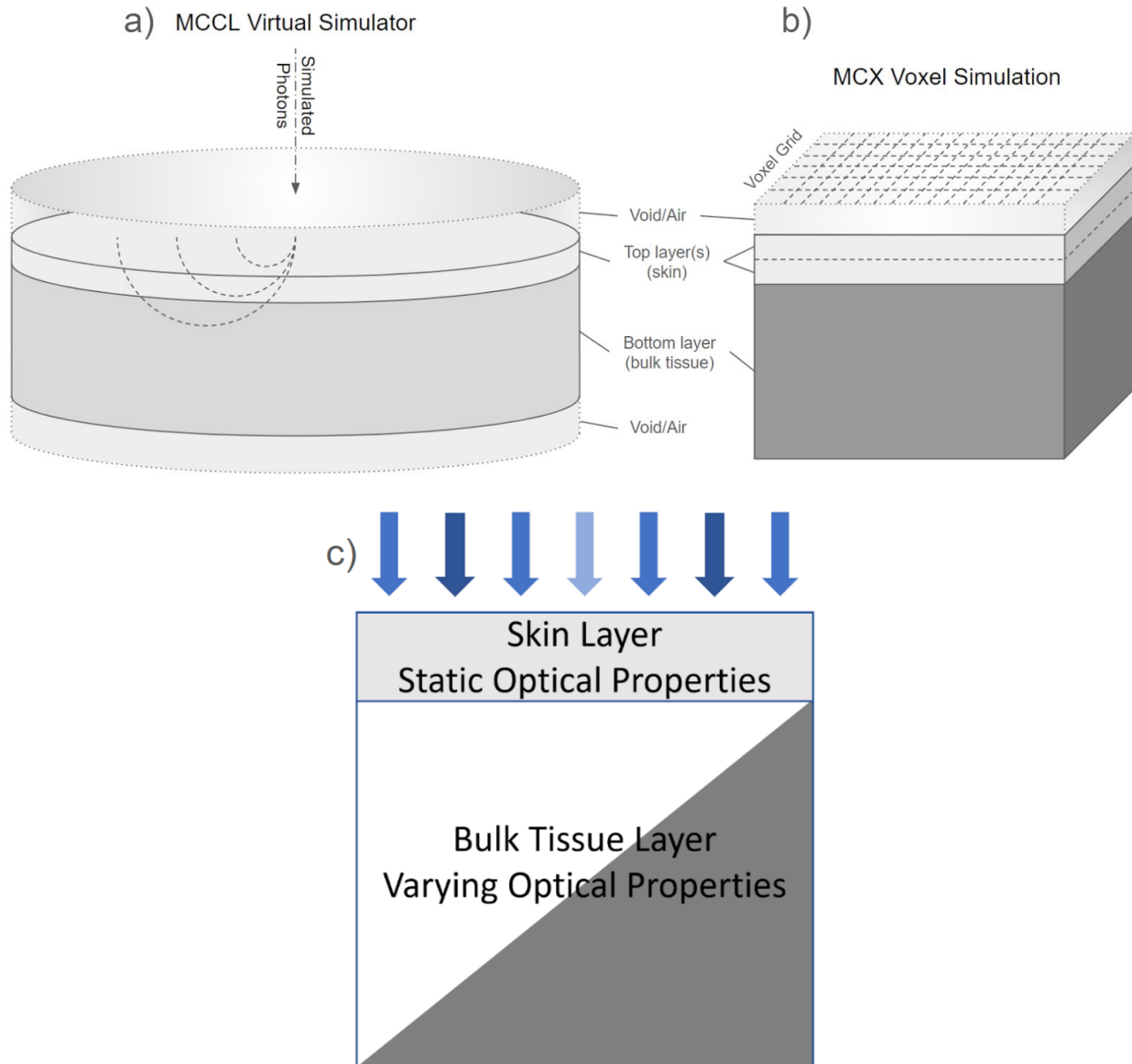
Figure 8a and 8b: Representative diagrams of the overall structure of MCCL and MCX tissue simulations. Fig 8c: representation of optical property setup of MCX and projected Fourier light intensity pattern.

While MCCL is capable of simulating either random photon absorption (sometimes called 'Russian roulette' simulation) or weighted photon 'packets' wherein the weight is reduced based on the absorption profiles of the tissue medium and pathlength, MCX by default works on the weighted photon packet model with only a marginal capacity to simulate total photon loss. This model is more reliable for acquiring detailed information with a lower photon count as each packet simulates many photons - the total photon losses in the simulation reduces effective photon simulation counts beyond those points of loss (and associated information), while the weighting model still retains the relevant information regarding likelihood of photon loss. This results in the photon packet model being a more computationally efficient method for the purposes of SFDI lookup table generation (Yan et al, 2020; Fang & Boas, 2009). Both MCCL and MCX are capable of simulating a large variety of photon sources, of which the 'pencil' and 'Fourier' source types are most relevant. The 'pencil' source simulates a pencil beam source and can be modeled by both MCCL and MCX, while only MCX is capable of modeling the 'Fourier' source, which projects a modulated 3-dimensional quadrilateral source with uniformly distributed but differentially weighted photon packets based on a specified spatial frequency pattern. This intensity distribution, which matches the projection patterns used for SFDI in clinical practice, is not possible to recreate in MCCL. Given this more direct modeling of SFDI imaging, the Fourier method may suffer from fewer potential sources of error, especially in a voxel-based simulation platform, enabling greater accuracy and speed in lookup table generation.

2.2.1 Gardner Method Implementation

To ensure that similar results could be achieved via MCX as with MCCL, we attempted several different methods to recreate the Gardner Method in MCX before settling on our present methodology. This would also allow further testing to take advantage of MCX's GPU acceleration for generating LUTs. As this project is a continuation of previous work, certain code was partially inherited from others, and the methods used to calculate R_d for the Gardner

method recreation displayed certain indiscrepancies compared to the results obtained by MCCL - it took multiple iterations of testing to realize that the origin of these inconsistencies was not a fundamental problem with recreating the Gardner method with MCXLAB's voxel-based simulations, but rather a mistake in post-processing calculations related to which axes were of interest (see Appendix for relevant code).

2.2.1.1 Comparison to MCCL Gardner Method

The Gardner method as originally described for photon weight calculations appears as shown in Equation 10, where W represents the photon's weight, μ_a represents the absorption coefficient of the simulated tissue layer, d represents the photon path length, f_x and f_y are spatial frequencies in the x and y axes respectively, and x_j and y_j are displacement of the photon's exit position from the origin in the x and y axes respectively.

Equation 10
$$W_j = e^{-\mu_a d} * e^{-2\pi i f_x x_j} * e^{-2\pi i f_y y_j}$$

As the spatial frequency was only non-zero for the x axis, the term for the y axis can be simplified to e^0 as any term multiplied by zero becomes zero. This then simplifies to the form shown in equation 11, as e^0 is equal to 1. This can be further adjusted to account for multiple layers if necessary, adding new terms multiplicatively to represent the absorption from each layer based on the absorption coefficient and total pathlength within that layer.

Equation 11
$$W_j = e^{-\mu_a d} * e^{-2\pi i f_x x_j}$$

This can be further simplified by using Euler's identity (see equation 12) to reduce the second term of Equation 10.

Equation 12
$$e^{ix} = cos\,(x) - i\,sin\,(x)$$

This reduced form can be seen in Equation 13, below:

Equation 13
$$e^{-2\pi i f_x x_j} = cos\,(2\pi\,f_x x_j) - i\,sin\,(2\pi\,f_x x_j)$$

Both the spatial frequency (f_x) and the displacement from the origin along a single axis (x_j) must be real numbers; as a result, their product with 2π will always be real as well. This

means that the second (sine) term of the reduced form seen in Equation 13 will always remain imaginary. As the data of interest lies wholly along the real axis, this imaginary component may be entirely ignored, resulting in the form shown in Equation 14.

Equation 14 $$W_j = e^{-\mu_a d} * cos(2\pi\, f_x x_j)$$

2.2.1.2 Simulated Tissue Phantom Dimensions

The phantom dimensions were structured to centralize around the light source at the center more, as was our detection method, using a large spherical detector. We used dimensions of 200mm x 200mm x 200mm (10mm voxels) when testing homogeneously or 100mm x 100mm x 40mm (1mm voxels) for multilayer tests, with 160 and 80mm radius detector spheres respectively. In Figure 9, which shows the simulated phantom, the wire outline indicates the edges of the voxel simulation, the red arrow indicates the origin and direction of simulated photons, and the green sphere represents the detector radius. Only photons which exit the bottom plane of the simulation inside the detector radius are detected, resulting in the oversized detector seen here to capture all relevant photons from one surface. Tissue layers are not visible due to absorption only being calculated as part of post-processing. Voxel size was less important to maintain as they were not being used as pixel collectors (demonstrably so, based on testing); using a single detector and bounding box detection - once a photon crosses out of the simulation space, the position of exit and other relevant information such as velocity and final weight are logged and the photon simulation is terminated.
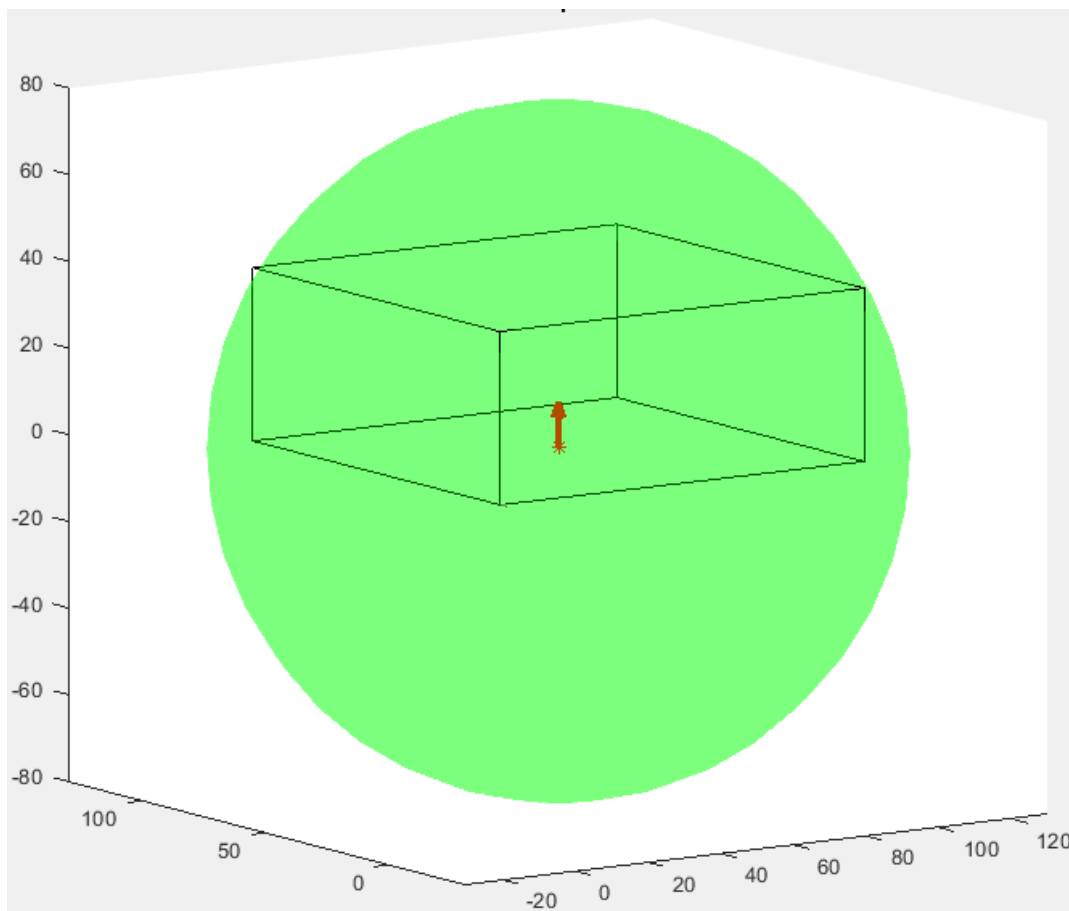
Fig. 9: Representation of Gardner method simulated tissue domain with detector and photon source in MCXLAB generated using mcxpreview.

2.2.2 Fourier Source Simulation(s)

The Fourier projection constructs the origin of the light source as an area and models spatial intensity by using different initial weights for photon packets based on specified frequency and the packet's unique starting position within that area (Yan et al, 2020). Figure 9c shows a very basic representation of this, with the color intensity of each blue arrow representing initial photon packet weight by position. This results in a simulated process directly analogous to clinical SFDI, including having to demodulate the output of the simulation to obtain finalized values - unlike the Gardner method, which does not require demodulation. Coding this demodulation process was the bulk of the difficulty in programming the Fourier method simulations (see Appendix for relevant code.

2.2.2.1 Simulated Tissue Phantom Dimensions

Though the initial simulated phantom was structured to be 100mm long, 60mm wide, and 20mm thick, with the projection area matching the x-y profile, testing revealed a significant drop in R_d values around the edges of the simulation in a manner dependent on simulated tissue phantom optical properties. This effect became negligible after adding a 20mm margin on either side to the simulation dimensions in the x and y planes, suggesting that the edge effect was due to simulated photons taking paths that would lead outside of the simulation, and resulting in overall dimensions for the simulation of 140mmx100mmx20mm. The projection area remained 100mm by 60mm; as by restricting the projection area to an integer number of spatial frequency cycles, the total power/area for a given photon count could remain constant across different simulations. Figure 10 shows this in more detail; the wire outline indicates the edges of the voxel simulation, the red arrow indicates the direction of simulated photons, the colored volumes indicate layers with different optical property values (purple: bulk tissue layer; green: skin layer), and the gray rectangle represents the light projection origin area.
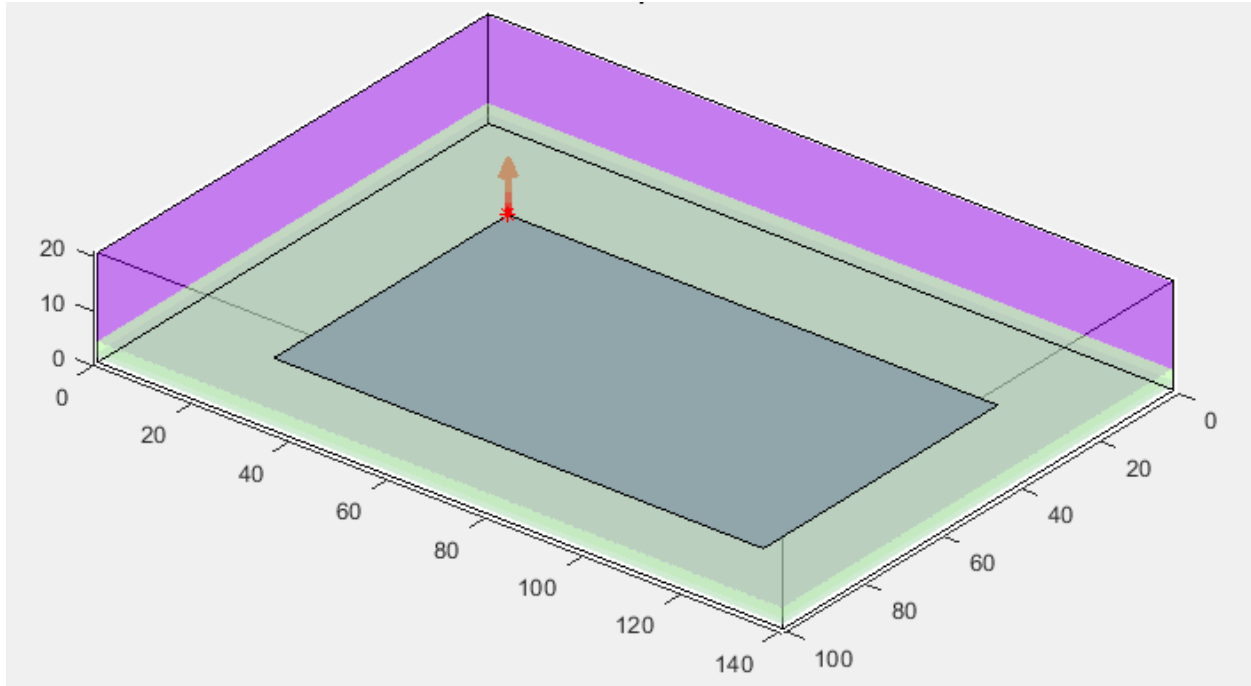
Fig. 10: Representation of Fourier method simulated tissue domain with detector and photon source in MCXLAB generated using mcxpreview.

2.2.2.2 Demodulation & R_d Calculation

While MCXLAB comes with certain ready-made functions to calculate diffuse reflectance while performing simulations, they are not always suitable for use for all applications. We used mcxcwdref.m, a function for computing continuous wave (CW) diffuse reflectance using the detectors system, as a basis to write a new function, mcxcwbbdref.m, designed to use bounding box detectors in place of spherical/point detectors. However, after significant testing and comparison with a third alternative method ('zero-layer' detection), we found that while using bounding box detection was able to capture additional information about simulated photons upon tissue exit (such as photon velocity vector, momentum transfer, and scattering event counts), it also increased the computational burden and coding complexity significantly, and our study's aims were unable to benefit from the additional information provided. As such, we opted to use zero-layer detection instead.

Zero-layer detection makes use of an MCX feature wherein diffuse reflectance or transmittance data can be saved in boundary voxels upon a simulated photon's exit from the simulation area at that boundary when the appropriate config variable is set (cfg.issaveref=1) and those boundary voxels have all properties set to 0. Each boundary voxel saves the photon packet weights of simulated photons that exit the simulated tissue into the voxel's local volume of simulation space as a negative sum, terminating the simulated photon packets after their weight is recorded. This conveniently bins the recorded photon weights into a pixel-like format, allowing ready use of pixel-by-pixel demodulation approaches (see Equation 1).

We wrote mcxdemodRd.m (see Appendix) to process the resulting information, which normalizes the recorded phase-pixel intensities based on the total applied photon density (photons per surface voxel within the projection area) using a procedure heavily based on methods suggested by one of Dr. Qianfang's students (Ragunathan, 2021), before demodulating using Equation 15, shown here for reference.

Equation 15

$$AC(x, y) = \frac{\sqrt{2}}{3} \{[I_{0°}(x, y) - I_{120°}(x, y)]^2 + [I_{120°}(x, y) - I_{240°}(x, y)]^2 + [I_{240°}(x, y) - I_{0°}(x, y)]^2\}^{1/2}$$

While the Gardner approach calculates the reduced photon weights from absorbance and pathlength after the fact so that multiple spatial frequencies can share the same initial simulation, cutting down on number of required simulations at the cost of additional post-processing computation load, the Fourier approach takes advantage of the increased computational power afforded by modern GPUs to reduce the photon weight with each photon, and recreates the demodulation process by directly modeling SFDI projection patterns.

CHAPTER 3

SIMULATIONS

A variety of tissue optical properties were simulated, based on previous work by

Tabassum et al. (Tabassum et al, 2018) to enable comparisons, available optical phantoms,

and known/calculated optical properties of human epidermal, dermal, and subdermal tissue

based on the work of Meglinski & Matcher, Lister et al., and the Oregon Medical Laser Center

w/ Steven Jacques (Meglinski & Matcher, 2002; Lister et al 2012; Jacques 2018); each relevant

method will detail the relevant optical properties.

3.1 MCX and MCCL Behavioral Comparison

MCCL was used to run several simulations using the Gardner method across a total of

fifty-one spatial frequencies (applied using post-processing) evenly distributed from 0.0 mm^{-1} to

0.50 mm^{-1} inclusive in 0.01 mm^{-1} increments on four different homogenous simulated tissue

phantoms with defined L^* values of 0.5, 1.0, 2.0, and 4.0, with a constant ratio of $\mu_s':\mu_a$ of 1:100.

Fifty-one spatial frequencies were generated due to the computational requirements of MCCL,

as this would allow the results of this generation process to be used in later tests as well.

MCXLAB was used to run several simulations with 1e7 photons across a total of ten key

spatial frequencies (0.0, 0.167, 0.333, 0.05, 0.10, 0.15, 0.20, 0.30, 0.40, and 0.50 in mm^{-1}) on

four different homogenous simulated tissue phantoms with defined L* values of 0.5, 1.0, 2.0,

and 4.0, with a constant ratio of $\mu_s':\mu_a$ of 1:100, using both Fourier and Gardner simulation

methods (spatial frequencies applied using post-processing for Gardner method, per standard

practice).

MATLAB was used to generate a set of diffusion approximations on homogenous

simulated tissue mediums using diffApproxSFD.m (see Appendix; adapted from Cuccia et al,

2009), for comparison purposes. These were performed across a total of ten spatial frequencies

(0.0, 0.167, 0.333, 0.05, 0.10, 0.15, 0.20, 0.30, 0.40, and 0.50) on four different sets of

homogenous simulated tissue characteristics with defined L* values of 0.5, 1.0, 2.0, and 4.0, with a constant ratio of $\mu_s':\mu_a$ of 1:100.

Table 2: Comparative Simulation Parameters

Simulation Method	F_x	L*	Photon #	Voxel Size
MCCL	0 to 0.50 (ten)	0.5, 1.0, 2.0, 4.0	1e7	1mm
Fourier	0 to 0.50 (ten)	0.5, 1.0, 2.0, 4.0	1e5	1mm
Fourier	0 to 0.50 (ten)	0.5, 1.0, 2.0, 4.0	1e7	1mm
Fourier	0 to 0.50 (ten)	0.5, 1.0, 2.0, 4.0	1e9	1mm
Gardner	0 to 0.50 (ten)	0.5, 1.0, 2.0, 4.0	1e5	1mm
Gardner	0 to 0.50 (ten)	0.5, 1.0, 2.0, 4.0	1e7	1mm
Fourier	0 to 0.50 (ten)	0.5, 1.0, 2.0, 4.0	1e7	0.5mm
Fourier	0 to 0.50 (ten)	0.5, 1.0, 2.0, 4.0	4e7	0.5mm
Diff Approx	0 to 0.50 (ten)	NA	NA	NA

Table 3: OPs Of Defined L* Values

L*	μ_a	μ_s'	μ_s (g=0.71)
0.5	0.0198	1.98	6.828
1.0	0.00990	0.99	3.414
2.0	0.00495	0.495	1.707
4.0	0.002475	0.2475	0.8535

3.1.1 Comparison between MC Simulation Results and Diffusion Approximation by

Spatial Frequency
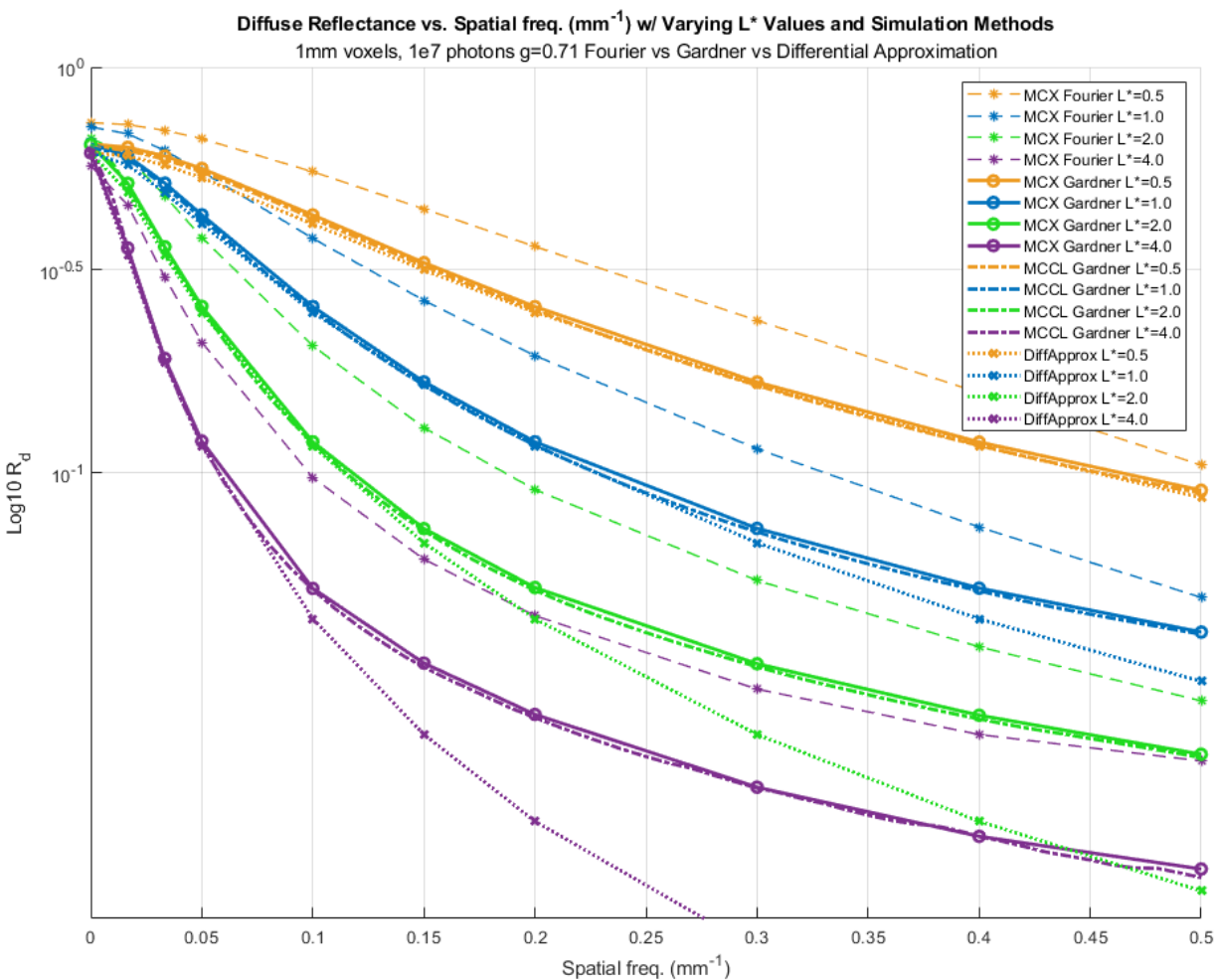
Fig. 11: Comparison of simulation results using a Fourier source approach with Monte Carlo

Extreme (MCX), Gardner method approach using MCX, Gardner method approach using

MCCL, and the Diffusion Approximation Equation.

For Figures 11-14, diffuse reflectance (R_d) is displayed as a function of spatial frequency

(fx) for varying L* values at a constant ratio of $\mu s / \mu a = 100$.

Figure 11 serves to illustrate the similarities and differences between simulation

methods. These results clearly demonstrate the high level of similarity between MCX Gardner

and MCCL Gardner approaches, as well as their divergence from diffusion approximation at

higher spatial frequencies and L* values, indicative of the limitations of an approximation-based approach (Khan et al, 2021). The use of a Fourier-source based approach produces very different results, with the overall changes being dependent both on spatial frequency and L* value. Importantly, it is not immediately obvious if the Fourier or Gardner approach would be more suitable for LUT generation in practice, given their differing levels of adherence to a theoretical model. Due to the more direct analogy to the clinical practice in the Fourier simulation, the alterations made may be a closer approximation of a practical scenario.

3.2 Comparative Performance of Fourier & Gardner Simulation Methodologies with Varying Photon Counts

Further simulations with 1e5 (Gardner & Fourier) and 1e9 (Fourier) photon counts were run for comparison of the effects of photon count changes with the previously mentioned spatial frequencies and simulated tissue phantoms.

3.2.1 Comparison Between MCX Simulation Results by Simulated Photon Density
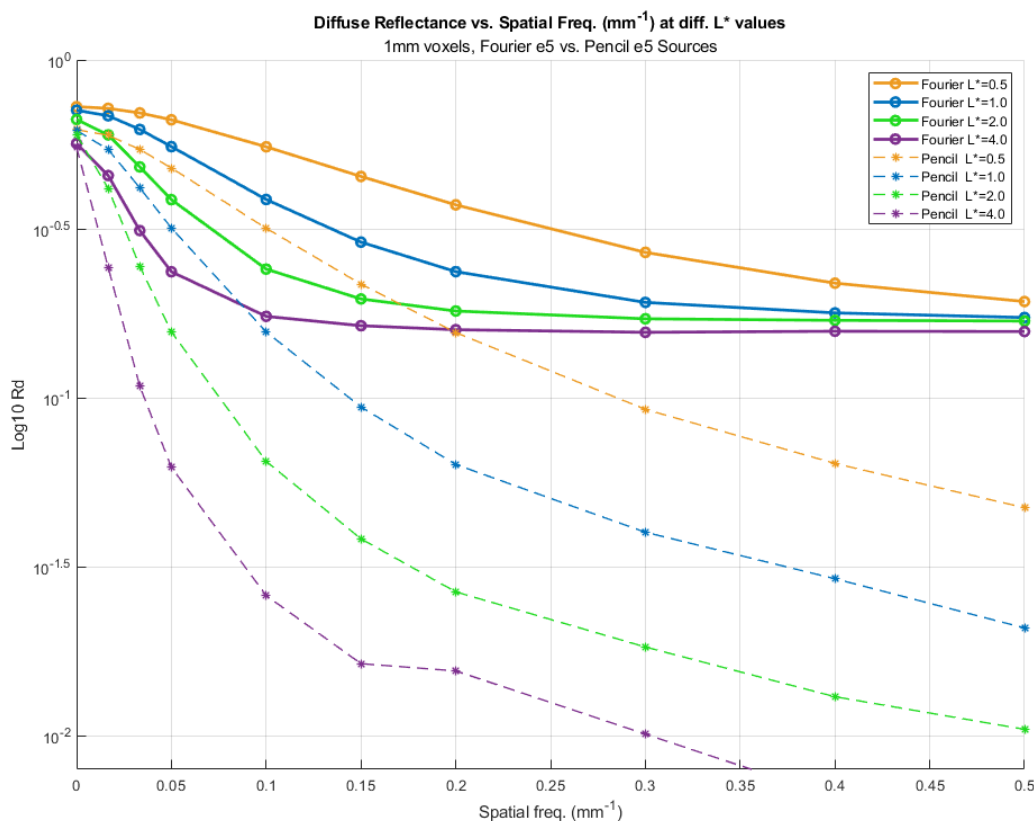
Fig. 12: Comparison of simulation results using Fourier source and Gardner method approaches with MCX at a reduced simulated photon count (10^5) and g=0.9.

We then tested the effects of altered photon counts for simulation on the MCX Fourier and MCX Gardner methods, shown in Figures 12-13; Figure 13b lacks a simulation of the Gardner method in MCX using 10^9 photons due to the extraordinary memory requirements this entailed. In conjunction with previous comparisons of Fourier vs. Gardner with identical photon counts (see Figure 12), these results demonstrate that while Gardner is less sensitive to a reduced photon count, the post-processing memory requirements pose issues for attempting to elevate the overall number of simulated photons The Fourier approach, though requiring a higher baseline to avoid a 'plateau' effect at high spatial frequencies, can continue to benefit from improvements in computational power for further increases in the number of simulated photons.
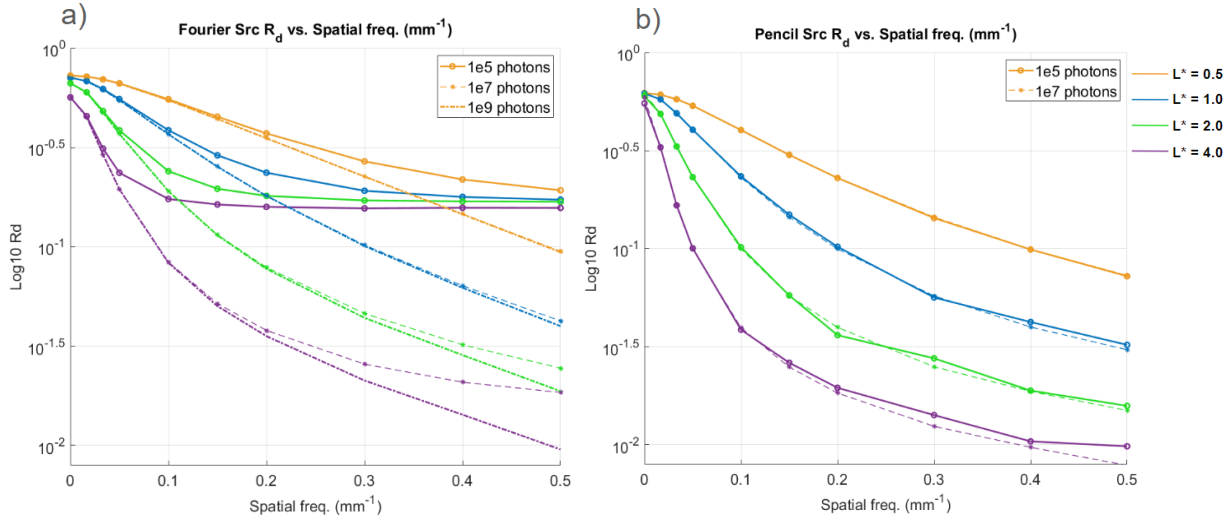
Fig. 13. a) Comparison of simulation results using a Fourier source approach with MCX at several different simulated photon counts (10^5, 10^7, and 10^9). b) Comparison of simulation results using a Gardner method approach with MCX at two different simulated photon counts (10^5 vs 10^7).

3.3 Effects of Reduced Voxel Scaling on Fourier Method

We performed simulations with the Fourier method using previously mentioned simulated tissue phantoms and spatial frequencies, with an anisotropy factor of 0.71, using 1e7 photons with 1mm voxels, 1e7 photons with 0.5mm voxels, and 4e7 photons with 0.5mm voxels, in order to test the effects of altered voxel size to investigate the capacity for more direct simulations of skin layers at their approximate thickness, as well as if these effects could be ameliorated by increasing the photon count proportionally to maintain cross-sectional area density of photons vs bin count for diffuse reflectance determinations. Due to the relationship between linear and area dimensions, a halving of voxel size results in a quadrupling of cross-section voxel count, resulting in the quadrupling of photon count to test cross-sectional photon density compensation. As illustrated in Figure 14: the ratio of photon count to voxels per horizontal layer is identical for 1.0mm voxels with 1e7 photons and 0.5mm voxels with 4e7 photons, but reduced by a factor of 4 for the 0.5mm voxels with 1e7 photons tests.
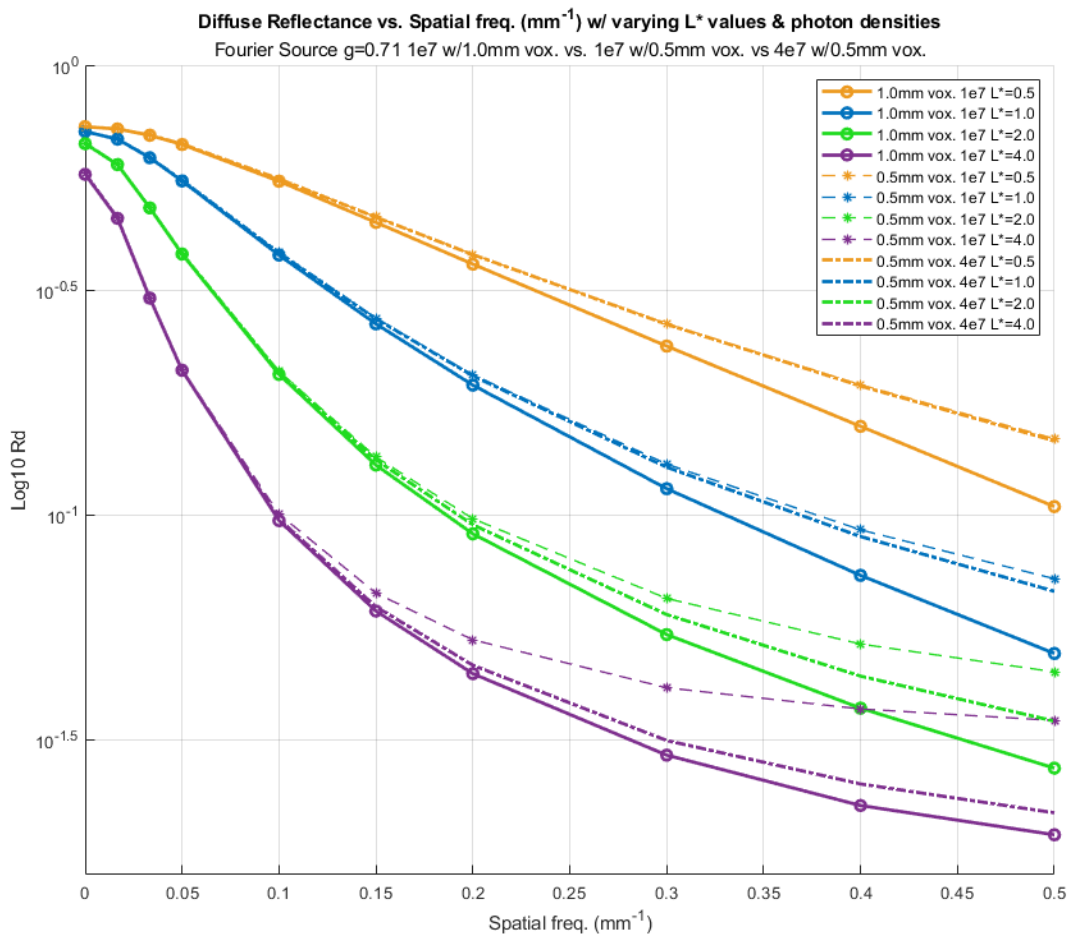
Fig 14: Comparison of simulation results using a Fourier source approach with MCX at different photon counts.

The results show that reduced voxel size makes a significant difference, as expected, due to the pixel-by-pixel demodulation process which is severely impacted by noisy data; smaller voxels results in smaller 'pixels' which means more numerous bins with fewer photons each, resulting in a reduction in accuracy. Increasing the photon count accordingly only helps at higher L* values (anticipated path-lengths), as the total propensity for noise in the data is still increased by the more numerous bins exacerbating small differences in photon endpoints. Figure 14 also points towards a cause for the plateauing effect demonstrated previously with higher l* values at higher spatial frequencies with insufficient photon counts - both higher spatial frequency and higher l* values present more opportunities for noise with a greater change in photon intensity projected over a given area and a longer photon path creating more possible

endpoints. As reduced voxel size - with associated increase in voxel count via linear-cubic relationship - rapidly balloons memory requirements for simulation, the associated requirement to simulate additional photons to maintain a similar density of simulated photons per voxel layer increases computational requirements significantly, such that further reductions in voxel size placed a very significant strain on available resources for simulation, up to and including frequent computer crashes. As MCX is intended for easy implementation on personal computers, laptops, and readily available lab computational resources, this analysis conducted no further tests along this line of inquiry. Skin layer tests were thus performed with an applied optical property weighting factor to account for the altered layer thickness in the simulation such that encountered scattering and absorption effects should match (as scattering and absorption coefficients are measured per unit distance) (Meglinski & Matcher, 2007).

3.4 Comparative Speed Performance of MCX and MCCL

MCCL, MCX Gardner, and MCX Fourier were used to run several simulations across a total of 51 spatial frequencies uniformly distributed from 0 to $0.50mm^{-1}$ on four different homogenous simulated tissue phantoms with defined L* values of 0.5, 1.0, 2.0, and 4.0, with a constant ratio of $\mu_s':\mu_a$ of 1:100 to determine relative times required for similar computations.

3.4.1 Comparison between MC Simulation Computation Time Requirements

We next tested the performance of MCX compared to MCCL in terms of computational time requirements for a range of 51 spatial frequencies evenly distributed from $0.0mm^{-1}$ to $0.5mm^{-1}$ across a range of simulated tissue optical properties based on established L* values. Table 1 demonstrates the significant advantages in performance offered by MCX's GPU acceleration and voxel-based simulations, (~114x speed boost at L*=0.5; ~24x speed boost at L*=4). This offers a clear advantage in using MCX for generating LUTs using higher photon counts, and/or generating a greater number of LUTs so as to cover a wider variety of situations.

As the Gardner method implemented in MCX here has a shorter runtime (Table 4) than an equivalent simulation performed using MCCL Gardner while producing nearly identical

results, the following elements of this analysis will be focused on the results of the MCX

Gardner and MCX Fourier based simulation approaches and the behavior of LUT inversion

algorithms based on these results.

Table 4: Comparative Time Trial Performance for 51-Frequency Runs

L* Val	MCX Fourier	MCX Gardner	MCCL Gardner
0.5	382.56 sec	141.25 sec	43614.75 sec
1.0	233.42 sec	122.73 sec	19311.29 sec
2.0	158.37 sec	99.92 sec	8360.78 sec
4.0	122.45 sec	87.27 sec	2941.06 sec

Table 4: Representative time trials of 51-frequency runs of 1e7 photon count simulations.

Simulations using lower l* values take longer as a result of higher scattering coefficients

resulting in a greater number of scattering events and attendant calculations; MCX Fourier is

more impacted as a result of the computational cost of simulations dominate computational

resource costs as compared to the level of post-processing required by MCX Gardner.

3.5 Homogenous LUT Generation

The MCX Fourier approach and the Gardner method in MCX were each used to

construct a set of LUTs based on simulated homogenous tissue phantoms. The physical

parameters of the simulated tissue phantoms used to produce these LUTs are shown in Table

5. The generation process was used for iterative testing to find suitable geometric parameters

and ensure effective MCXLAB implementation of the LUT generation process for both methods,

with a final set of generated homogenous LUTs used alongside an extant popular MCCL

Gardner method-based homogenous LUT (LUT_Homogenous_Large_1e6.mat) to extract

optical properties from an available physical homogenous tissue phantom imaged with via

VISNIR using a Modulim Reflect RS and these extracted optical properties compared to DOSI

determined optical properties to ensure practical applicability and test relative accuracy.

Table 5: Homogenous Simulated Tissue Phantom Properties

Parameters	Fourier	MCX Gardner	MCCL Gardner
Photon #	1e7	1e7	1e6
Spatial Frequencies (mm^{-1})	0.0, 0.1	0.0, 0.1	0.0, 0.1
n	1.4	1.4	1.4
g	0.82	0.82	0.82
μ_a	0 - 0.2 (100 steps)	0 - 0.2 (100 steps)	0 - 0.5 (400 steps)
μ_s'	0.01 - 5.0 (100 steps)	0.01 - 5.0 (100 steps)	0.2 - 7.0 (300 steps)
Voxel size	1mm	10mm	N/A
Simulated Tissue Phantom Dimensions	140mm x 100mm x 20mm	200mm x 200mm x 200mm	N/A
Illuminated Area	100mm x 60mm	N/A	N/A

3.6 Multilayer LUT Generation and Comparison of Gardner & Fourier Methods

The MCX Fourier approach used a three-layer system wherein the top layer represents the epidermis with μ_a and μ_s' values weighted based on relative thickness compared to the voxel sizes used, the middle layer represents the dermis with fixed optical properties with fixed μ_a and μ_s' values weighted based on similar metrics, and the bottom layer represents a significantly thicker adipose tissue adequately comparable to the semi-infinite tissue layers used in other multi-layer SFDI studies. The Gardner method used a two-layer system similar to previous work with only a skin layer and an adipose tissue layer. Table 6 shows the optical properties of the various layers used, as well as the modeled thickness (theoretic thickness being simulated) and the voxel depth (actual depth of voxels used to represent the layer for the simulation)

Table 6: Multilayer LUT Layer Specifications

Layer	μ_a	μ_s	n	g	modeled thickness (mm)	voxel depth
Fourier dynamic adipose (bottom) layer	0 - 0.20	0.01 - 5.0	1.4	0.82	16	16
Fourier static dermis (middle) layer	0.04292	2.267	1.4	0.82	1.8	2
Fourier light epidermis (top) layer (3% mel.)	0.66766	6.413	1.4	0.82	0.1	1
Fourier dark epidermis (top) layer (42% mel.)	9.10784	6.413	1.4	0.82	0.1	1
Gardner dynamic adipose (bottom) layer	0 - 0.20	0.01 - 5.0	1.4	0.82	39	39
Gardner light epidermis (bottom) layer (3% mel.)	0.66766	6.413	1.4	0.82	0.1	1
Gardner dark epidermis (bottom) layer (42% mel.)	9.10784	6.413	1.4	0.82	0.1	1
Fourier static bottom layer (DOSI-matched)	0.002793	6.49313	1.4	0.82	16	16
Fourier dynamic top layer	0 - 9.9	0 - 29.7	1.4	0.82	0.1	1

3.6.1 Comparison between MCX Multilayer Simulation Based LUT Inversion Algorithms:

Fourier vs Gardner
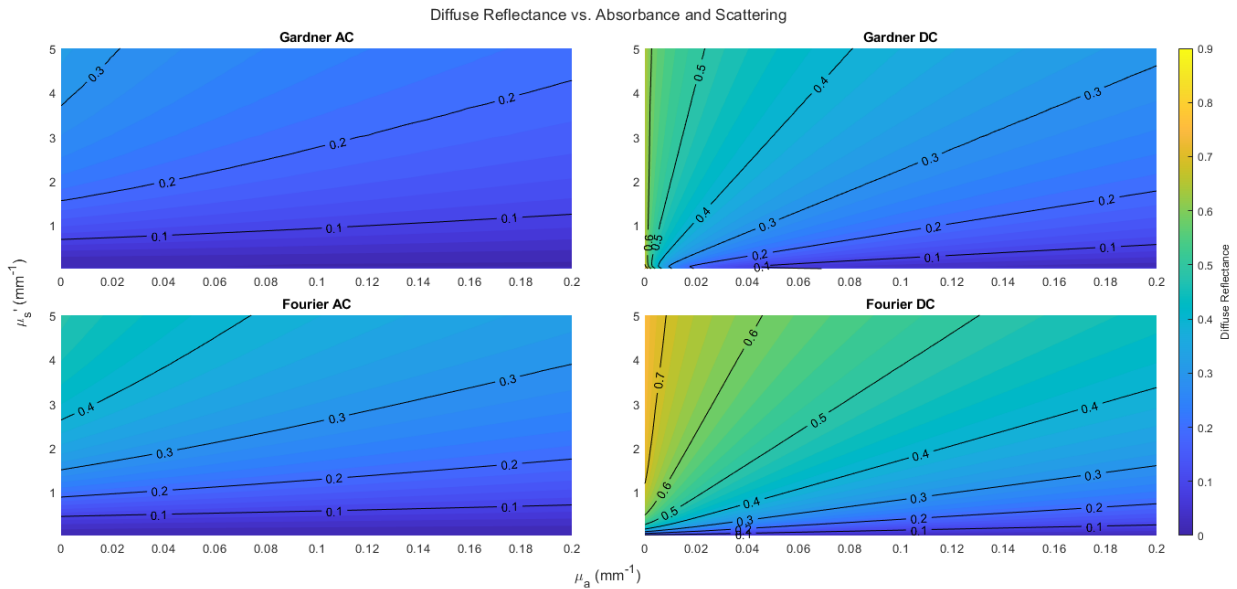
Figure 15: Comparison of LUT inversion algorithms based on three-layer Fourier source and two-layer MCX Gardner method approaches with a light simulated skin layer. (a) and (b) Optical properties versus AC R_d and DC R_d, respectively, for the MCX Gardner LUT. (c) and (d) Optical properties versus AC R_d and DC R_d, respectively, for the Fourier LUT.

For Figures 15, 18, 19, 23, and 24, R_d values are shown both in the color dimension and as labeled isolines for the entire range of simulated μ_a and μ'_s values.

For Figures 16, 20, and 21, optical property values (μ_a and μ'_s) are shown both in the color dimension and as labeled isolines for the entire range of resulting R_d values.

An example of the effects of simulation method on LUT inversion algorithms for a three-layer phantom using optical properties that simulate a lighter-skin tone (3% melanosome content) is shown in Figure 15, using two spatial frequencies and comparing Gardner method and Fourier source approaches in MCX. The Fourier and Gardner approaches demonstrate significant differences in coverage values but a very similar structure in the distribution pattern as shown by the isolines, with Fourier in particular covering a wider range of potential diffuse

reflectance values (approx. 0-0.71 vs approx. 0-0.6), suggesting a possible increase in specificity during OP extraction.

This appears to be confirmed by Figure 16, which compares the theoretic extracted/projected optical properties for every combination of diffuse reflectance values which the LUTs contain, with μ_a optical property extraction in particular being especially affected, particularly for high R_d values returned from planar sources (DC).
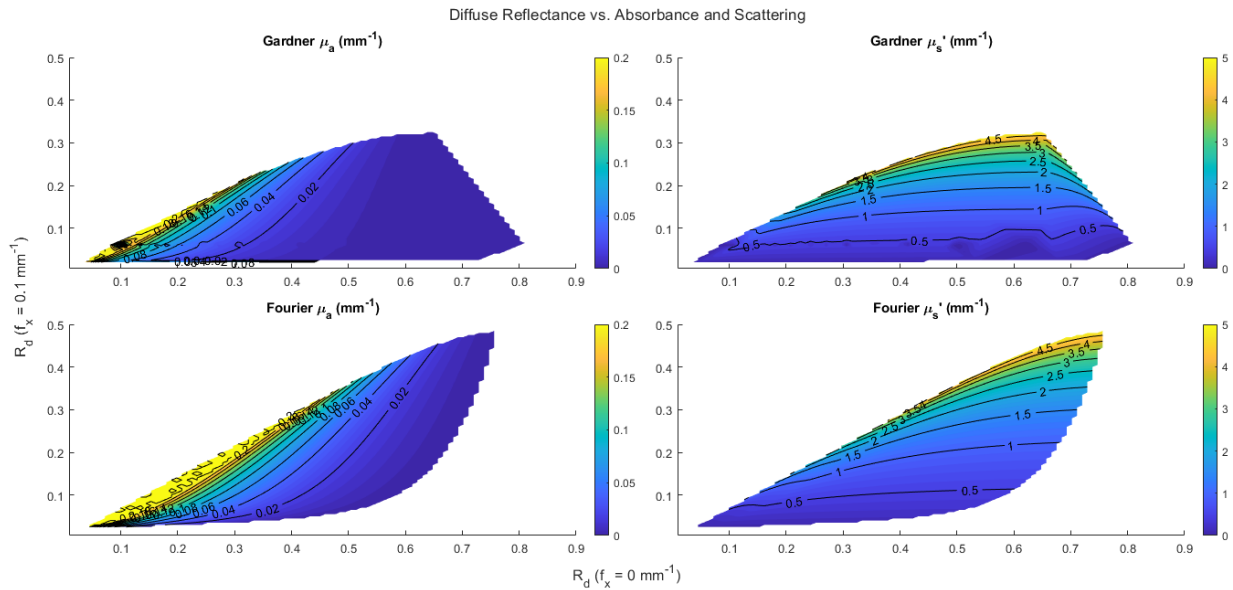
Figure 16: Comparison of optical property extractions using LUT inversion algorithms based on three-layer MCX Fourier source and two-layer MCX Gardner method approaches with light simulated skin layers. (a) and (b) R_d values versus μ_a and μ_s', respectively, for the MCX Gardner 2-layer LUT. (c) and (d) R_d values versus μ_a and μ_s', respectively, for the Fourier 3-layer LUT.

Figure 17 illustrates both the absolute and relative discrepancies between MCX Gardner and Fourier methods in their overlapping area, with the greatest differences appearing near the overlap region's borders, particularly the regions where the extracted optical properties are at their highest or lowest.
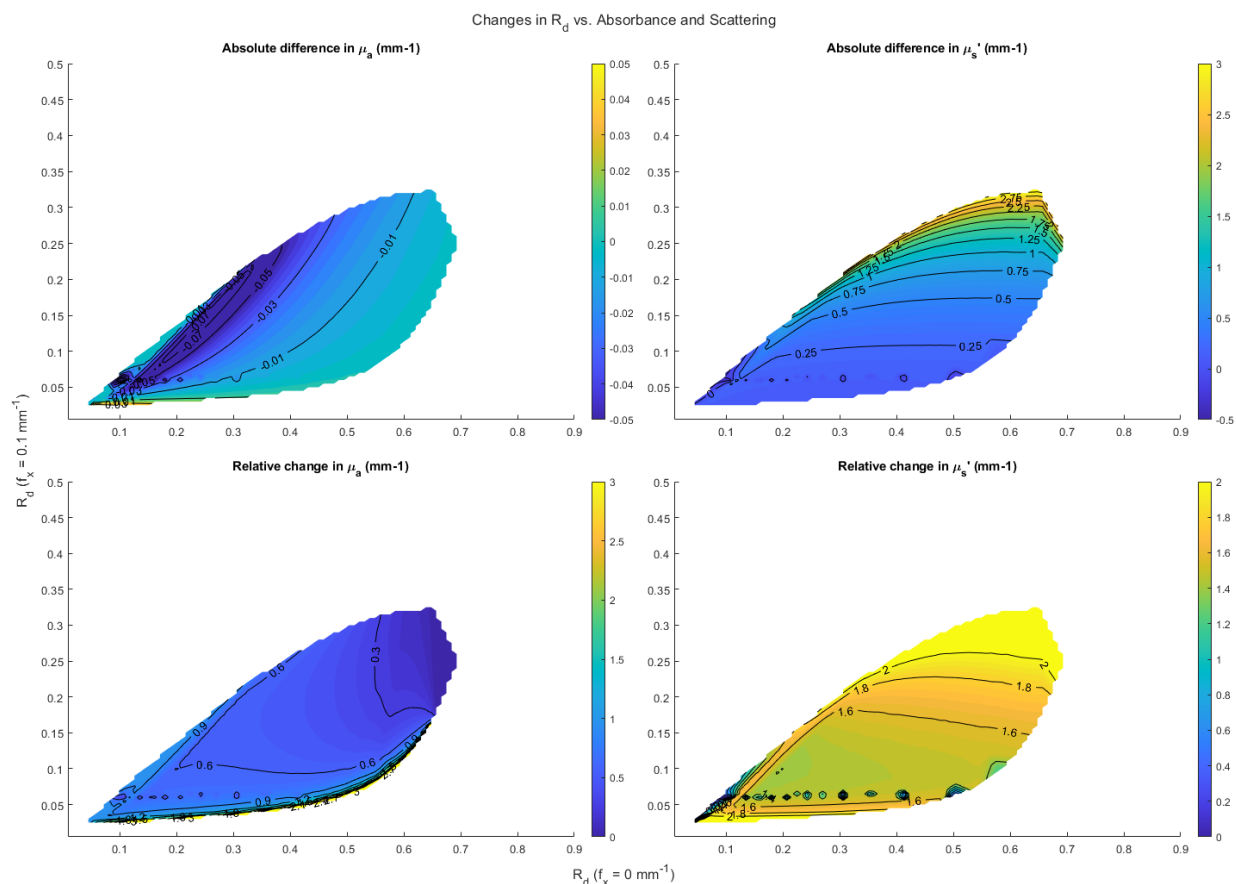
Figure 17: Impact on optical property extractions of the MCX Gardner two-layer LUT inversion algorithm shown as absolute and relative differences compared to the Fourier three-layer case, with light simulated skin layers. (a) and (b) Absolute differences in μ_a and μ'_s determinations, respectively. (c) and (d) Relative differences in μ_a and μ'_s determinations, respectively.

Figure 18 demonstrates that the relationship established by Figure 16 holds true when modeling a dark-skinned (42% melanosome content) epidermal model as well; the Fourier method demonstrates an improved dynamic range when modeling optical properties against diffuse reflectance values.
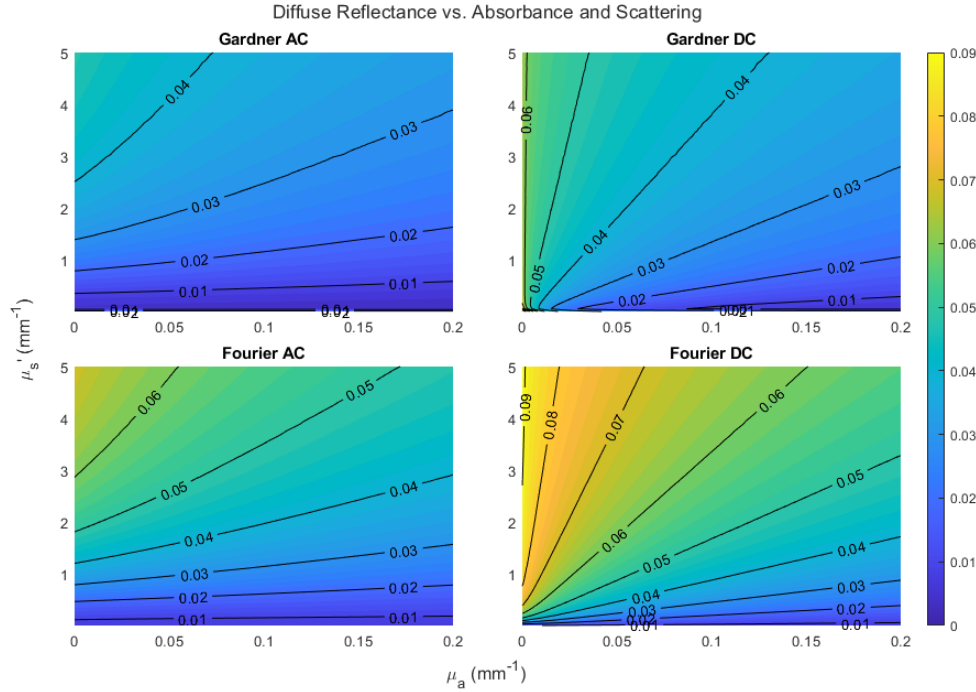
Figure 18: Comparison of LUT inversion algorithms based on three-layer MCX Fourier source and two-layer MCX Gardner method approaches with a dark simulated skin layer (42% melanosome content). (a) and (b) Optical properties versus AC R_d and DC R_d, respectively, for the dark skin MCX Gardner LUT. (c) and (d) Optical properties versus AC R_d and DC R_d, respectively, for the dark skin Fourier LUT.

3.7 Multilayer LUT Generation and Skin Type Comparison

The MCX Fourier approach and the Gardner method in MCX were each used to construct a set of LUTs based on simulated multi-layer tissue phantoms. These LUTs were produced using simulated tissue phantoms with physical parameters aimed to compare the effects of the generation method and assumed skin color on multi-layer LUTs (Table 6).

For these LUTs, the optical properties of the non-adipose layers were fixed based on existing known OPs of the dermis and epidermis given a specific melanosome concentration (Meglinski & Matcher, 2002), while the adipose (bulk layer) tissue optical properties serve as the free parameters of the inversion algorithm.

3.7.1 Comparison between MCX Fourier-source three-layer Simulation-Based LUT Inversion Algorithms: Light Skin vs Dark Skin
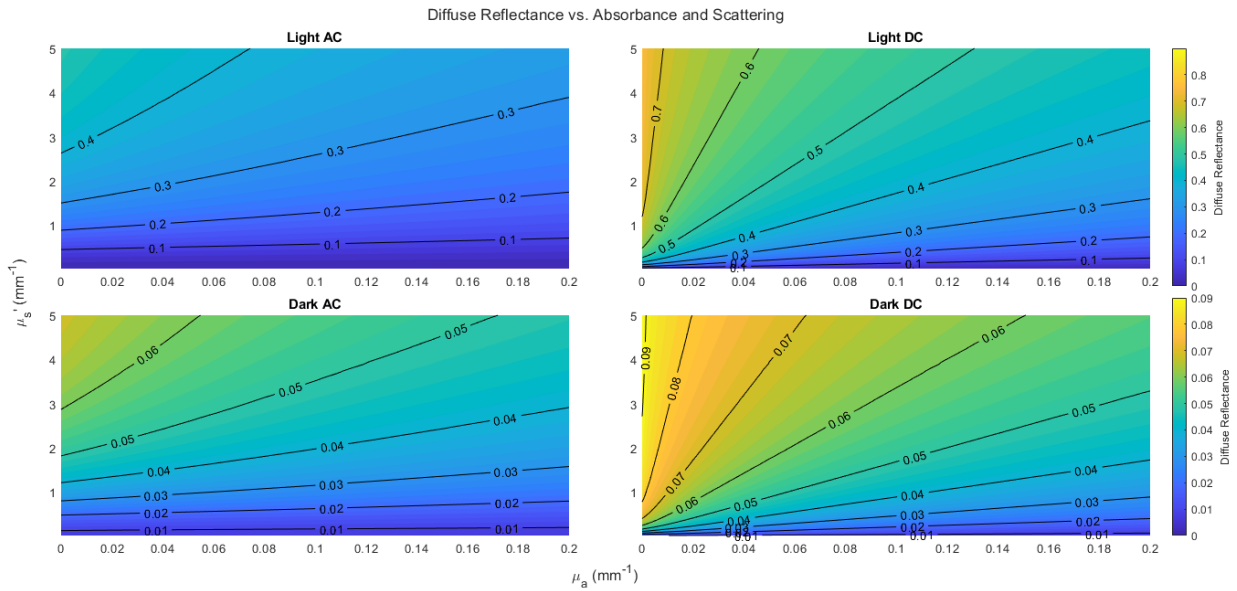
Figure 19: Comparison of LUT inversion algorithms based on three-layer MCX Fourier source method approaches with a light (melanosome content: 3%) and dark (melanosome content: 42%) simulated skin layer. (a) and (b) Optical properties versus AC R_d and DC R_d, respectively, for the light skin Fourier LUT. (c) and (d) Optical properties versus AC R_d and DC R_d, respectively, for the dark skin Fourier LUT.

To evaluate the necessity of discrete LUTs for different skin colors, we used MCX Fourier to compare LUTs generated using simulated tissues with optical properties based on low melanosome content versus high melanosome content epidermal tissue to examine the impacts of light skin versus dark skin on returned diffuse reflectance values. Figure 19 depicts a heatmap colorized version of the LUTs so generated, showing extremely dissimilar R_d values but with very similar structures of those values.
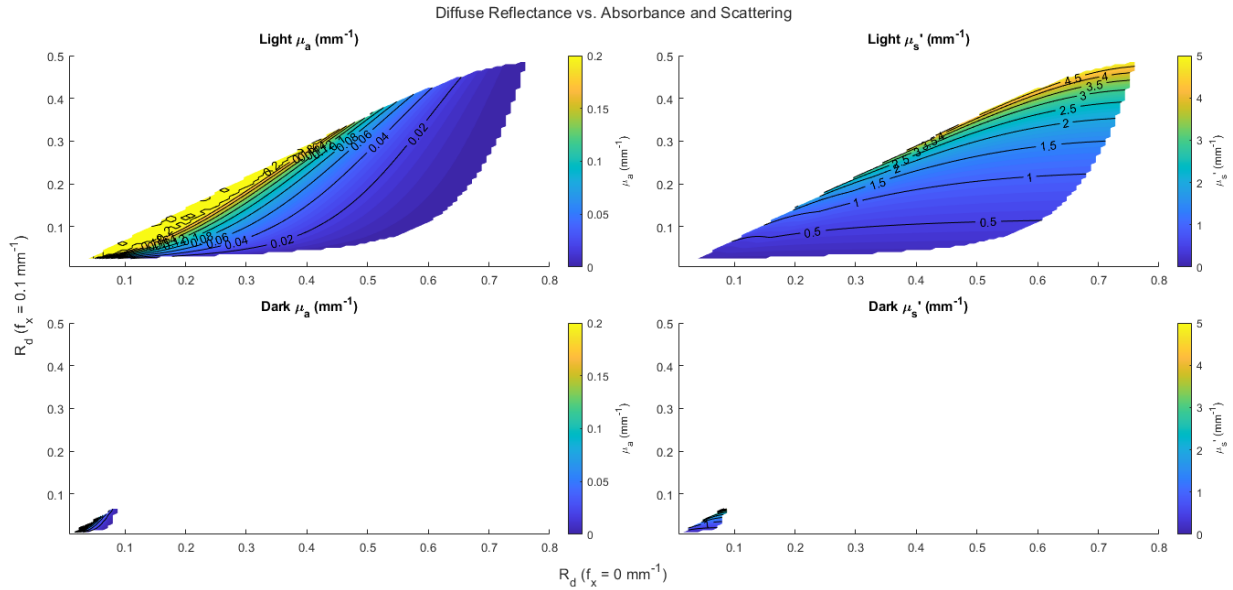
Figure 20: Comparison of lookup tables generated using dark (melanosome content: 42%) vs light (melanosome content: 3%) simulated skin layers in MCX. (a) and (b) R_d values versus μ_a and μ_s', respectively, for the light skin Fourier LUT. (c) and (d) R_d values versus μ_a and μ_s', respectively, for the dark skin Fourier LUT, with identical axis scaling.

Figures 20 and 21, which have optical properties matching to varying R_d values are shown for both AC and DC frequencies, demonstrate the significant differences in these LUTs. Both figures are of the same data, but Figure 20 uses proportional representation with identical scaling on axes between light and dark simulated skin layers, while Figure 21 uses scaled representation, expanding the axis scaling for the dark simulated skin layer. These also show, however, that this difference is primarily scalar, such that LUTs generated using optical properties based on dark skin should still function normally for individuals with matching complexions.
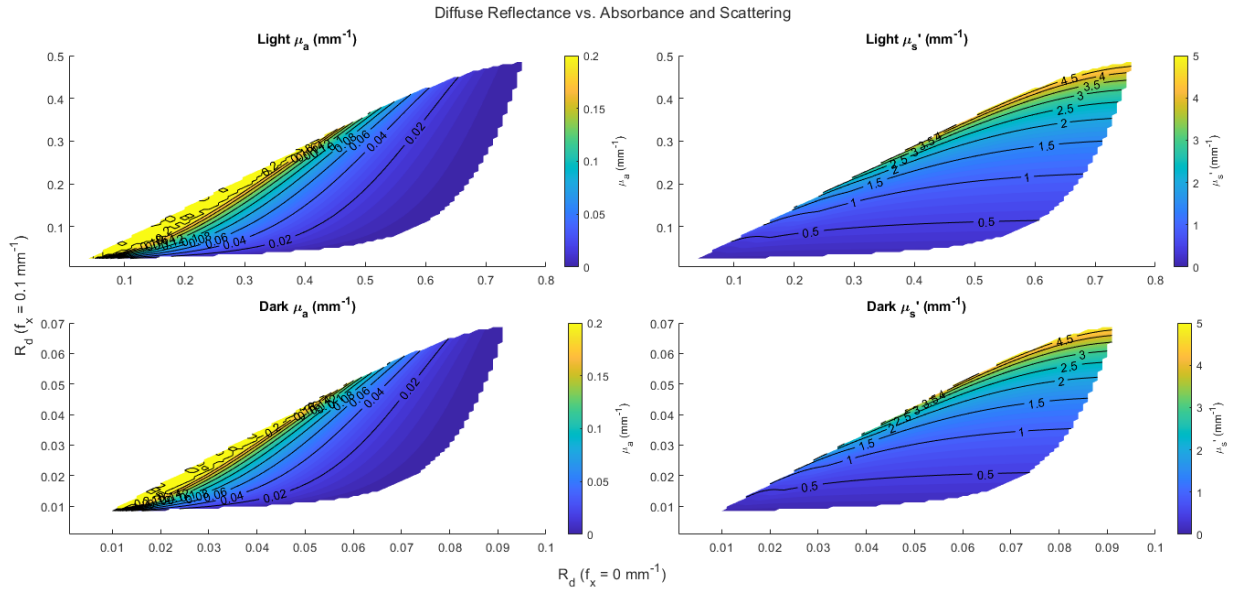
Figure 21: Comparison of lookup tables generated using dark (melanosome content: 42%) vs light (melanosome content: 3%) simulated skin layers in MCX. (a) and (b) R_d values versus μ_a and μ_s', respectively, for the light skin Fourier LUT. (c) and (d) R_d values versus μ_a and μ_s', respectively, for the dark skin Fourier LUT, with relative axis scaling.

Figure 22, generated by direct division of the light by the dark plots in Figure 19 and calculation of the standard deviation of the resulting plots, shows that for light (3%) vs dark (42%) melanosome content in the skin layers, the regions with the greatest divergence from this scalar pattern occur at extremely low values for μ_s' where the R_d values are lowest and μ_a would dominate; this is likely exacerbated due to the stochastic nature of photon scattering in such a regime resulting in a relatively elevated impact of noise. The mean of relative R_d values for Figure 22 was 7.875 with a standard deviation of 0.612 for the DC comparison, and 6.305 with a standard deviation of 0.913 for the AC comparison.
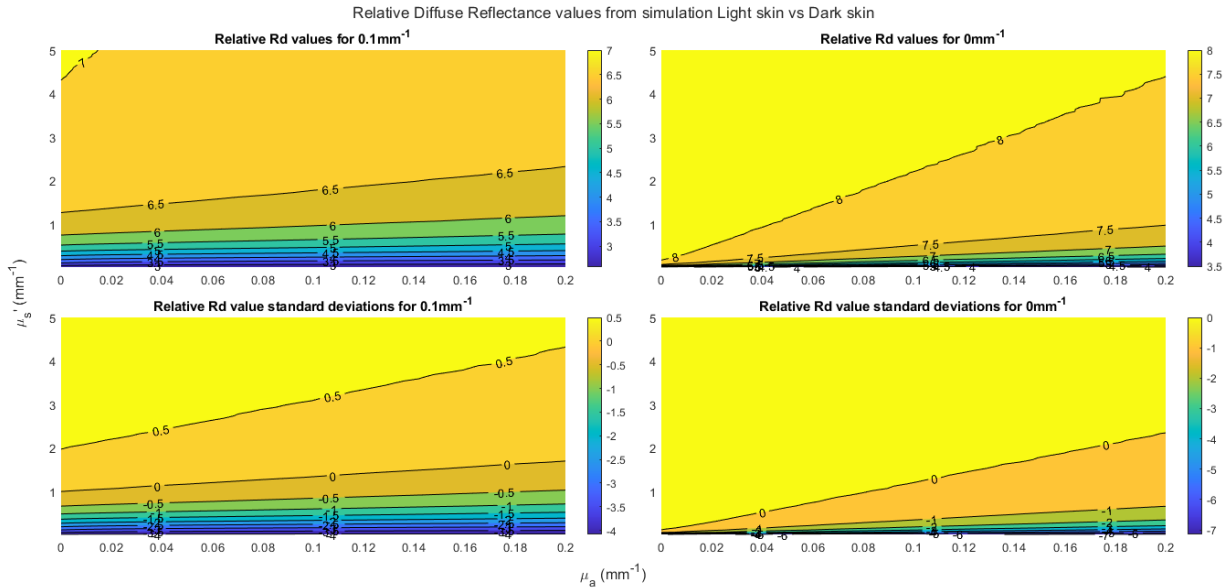
Figure 22: Comparison of relative LUT inversion algorithm output patterns based on three-layer MCX Fourier source method approaches with light vs dark simulated skin layers. (a) and (b) relative values of light vs dark skin Fourier LUT for AC R_d and DC R_d, respectively. (c) and (d) standard deviation values of plots (a) and (b), respectively.

3.8 Physical Tissue Phantom OP Extraction

We examined the performance of our LUT generation process by using the LUTs to process imaging data taken of real tissue phantoms and compare the resulting extracted optical properties to optical properties obtained through non-SFDI processes known to be reliable.

3.8.1 Roblyer Lab Phantoms (Homogenous & Two-Layer)

Multilayer phantom imaging data was provided by collaborating members of the Darren Roblyer lab with BOTlab, with DOSI-confirmed OPs for calibration phantom only, used to practically test lookup tables generated, esp. comparing different simulated skin type LUT-based extraction results for different multilayer phantoms vs. homogenous LUT against homogenous top and base layer phantoms. Imaging data provided consisted of 2 cm thick homogenous bulk tissue phantoms labeled bpav4, Skin2, Skin3, Skin4, Skin5, and Skin6, as well as images of combined tissue phantoms consisting of an approx. 2 millimeter thick skin layer on top of the bulk bpav4 phantom, for each skin tissue phantom provided.

3.8.2 Phantom Comparisons
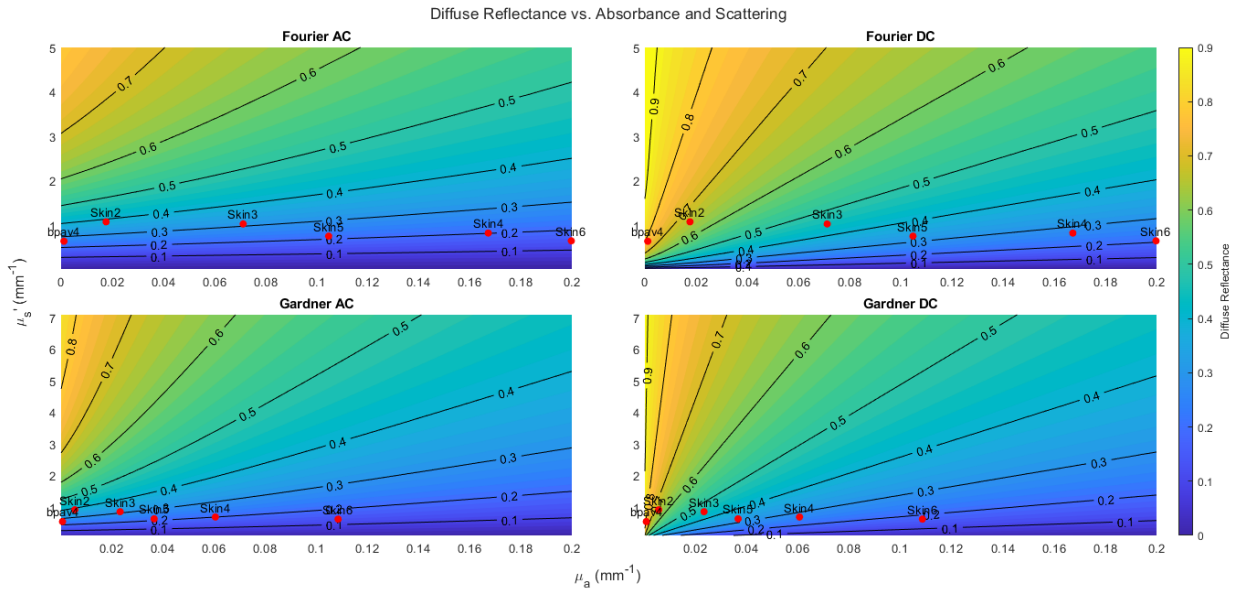
Figure 23: Comparison of LUT inversion algorithms based on homogenous Fourier source and MCX Gardner method approaches, overlaid by extracted Optical Property values of real tissue phantoms provided by the Roblyer lab shown here as red dots. (a) and (b) Optical properties versus AC R_d and DC R_d, respectively, for the Fourier LUT. (c) and (d) Optical properties versus AC R_d and DC R_d, respectively, for the MCX Gardner LUT.

Figures 23 and 24 show the extracted optical properties of collaborator-provisioned phantom imaging data processed with homogenous and multilayer Fourier and MCX Gardner based LUT inversion algorithms respectively, plotted against those same inversion algorithms for context. Without DOSI-provisioned data for comparison, only the relative positions of the homogenous and multilayer tissue setups serve as useful bases from which to draw meaningful conclusions from. The data showed unsurprising results: the multilayer tissue set-ups demonstrate a reduced overall absorption coefficient compared to the skin layers on top of them due to the thickness of the extremely low absorption bulk tissue phantom (bpav4), and an elevated scattering coefficient which may be the result of imperfect border between the bulk tissue phantom (bpav4) and the thin skin tissue phantoms, as they were distinct tissue phantoms, not cohesive blocks.
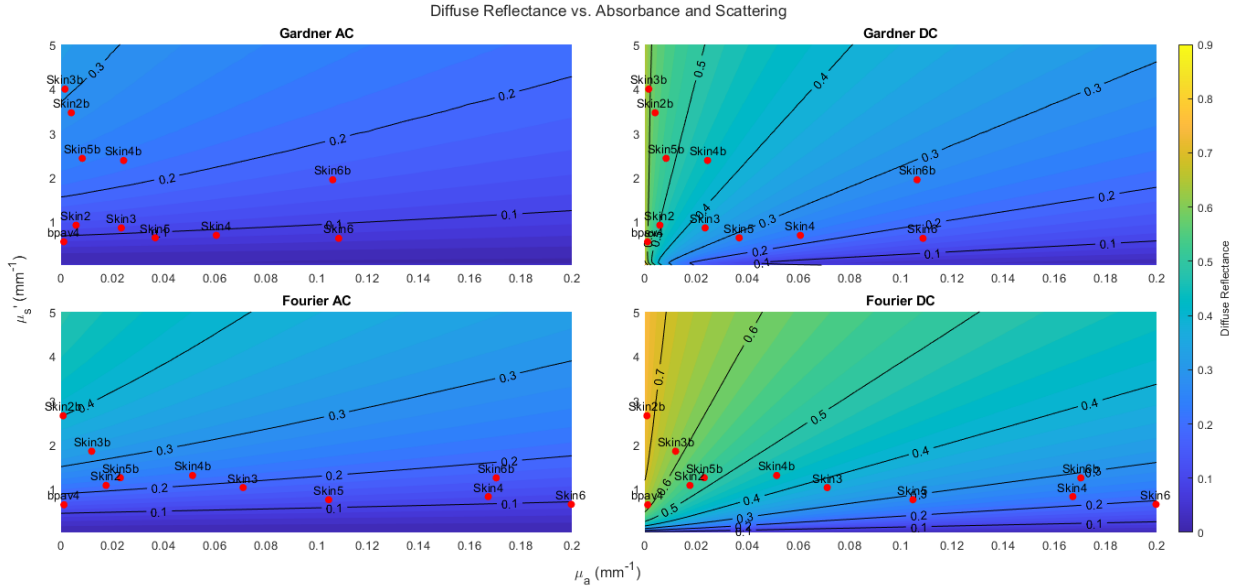
Figure 24: Comparison of LUT inversion algorithms based on three-layer Fourier source and three-layer MCX Gardner method approaches with a light simulated skin layer, overlaid by extracted Optical Property values of real tissue phantoms provided by [Roblyer Lab]. (a) and (b) Optical properties versus AC R_d and DC R_d, respectively, for the MCX Gardner LUT. (c) and (d) Optical properties versus AC R_d and DC R_d, respectively, for the Fourier LUT.

3.8.3 Tilbury Lab Phantoms (Homogenous)

Phantom imaging data for testing purposes was acquired in-house via VISNIR using Modulim Reflect RS (see Appendix for specifications). Using DOSI-confirmed optical properties as a comparison base allowed us to test error rates of homogenous single-layer LUTs generated with each method.

Table 7: Comparative Error Of Distinct LUT Generation Methods vs Real Tissue Phantom

LUT	λ	μ_a	μ_s'	GT μ_a	GT μ_s'	μ_a Error	μ_s' Error
MCCL Gardner	659	0.0071	1.4115	0.0027933	1.168783	154.2%	20.8%
MCCL Gardner	691	0.0069	1.3428	0.0027022	1.087909	155.3%	23.4%
MCCL Gardner	731	0.0069	1.263	0.0028155	0.999159	145.1%	26.4%
MCX Fourier	659	0.0037	0.9226	0.0027933	1.168783	32.5%	21.1%
MCX Fourier	691	0.0032	0.8796	0.0027022	1.087909	18.4%	19.1%
MCX Fourier	731	0.0029	0.8282	0.0028155	0.999159	3.0%	17.1%
MCX Gardner	659	0.0049	1.4989	0.0027933	1.168783	75.4%	28.2%
MCX Gardner	691	0.0046	1.4275	0.0027022	1.087909	70.2%	31.2%
MCX Gardner	731	0.0045	1.346	0.0028155	0.999159	59.8%	34.7%

Table 7 Caption: DOSI-derived values labeled with GT (ground truth).

In testing the performance of homogenous LUTs generated by MCX Fourier, MCX Gardner, and MCCL Gardner against real-world tissue phantoms against optical properties extracted by DOSI at key wavelengths, the MCX Fourier homogenous LUT demonstrates reduced error compared to MCX Gardner-based homogenous LUTs and previously preferred homogenous LUTs generated via MCCL, especially in absorption coefficient (μ_a) extraction,

confirming previous predictions of improved performance relative to MCX Gardner and the Gardner method more broadly.

3.9 Impacts of Inaccurate Multilayer LUT Skin Assumptions

To examine the relative accuracy of generated LUTs against various skin types, and the useful range of complexions a lookup table built with a particular set of assumptions regarding melanosome concentration in the epidermis is able to remain accurate for, a sensitivity analysis was conducted. By generating LUTs based on a variable top layer and a static base layer, rather than the static top layer and variable top layer as in previous/standard multilayer LUTs (see Figure 25), the sensitivity analysis is able to reflect the limited but significant impact of melanin, which, in human skin, is entirely concentrated in the epidermis, which the top layer of the simulated tissue phantom represents. The diffuse reflectance values for this variable top layer LUT were then treated as source data from which to attempt to extract optical properties using standard multilayer LUT models with varying top layer properties, with the expectation that differences between the top layer optical properties would result in varying levels of error in the extracted underlying optical properties of the underlying static layer. This was then used to calculate maximum acceptable deviances from true top layer properties and determine the useful range of lookup tables built with a given set of assumptions regarding top layer OPs, and accordingly, when new lookup tables must be generated to fit a patient's skin complexion.
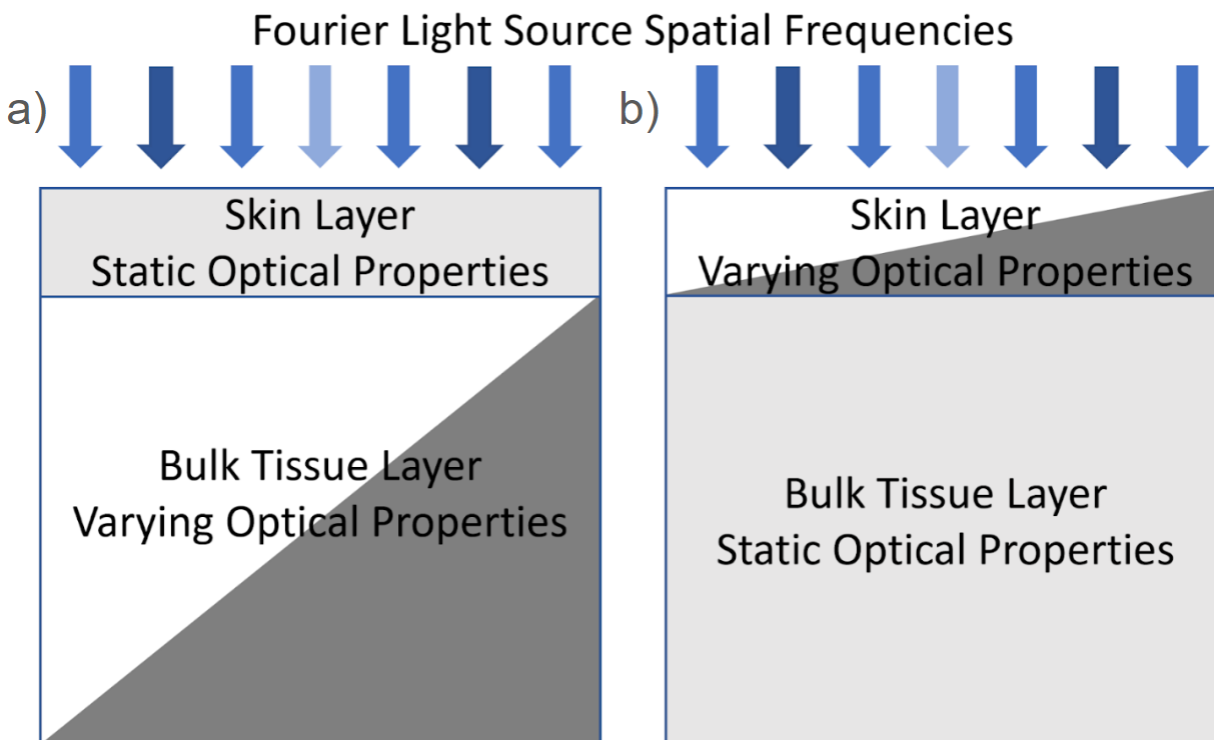
Fig. 25: Representation of the differences in approach for multilayer LUT tissue simulations with static or dynamic tissue layers. The tissue layer which has variable optical properties across the LUT is switched from the bottom bulk layer to the top layer (representing the epidermis), effectively simulating a wide range of skin types over static tissue. a) Standard multilayer LUT setup, with static top layer OPs over dynamic OPs of a bulk or flesh layer. b) Swapped multilayer LUT setup, with dynamic top layer OPs over a static set of OPs for the bulk or flesh layer.

To confirm the efficacy of this method, DOSI-confirmed values from an in-house tissue phantom were included to establish a known baseline for the static bulk layer (using the ground truth values in Table 7) of the simulated tissue phantom used in this sensitivity analysis; error in extracted OPs was treated as departure from these known values.

3.9.1 Sensitivity Analysis

For Figure 26, Rd values are shown both in the color dimension and as labeled isolines for the entire range of simulated μ_a and $\mu's$ values. For Figure 27, optical property values (μ_a

and μ's) are shown both in the color dimension and as labeled isolines for the entire range of resulting Rd values.
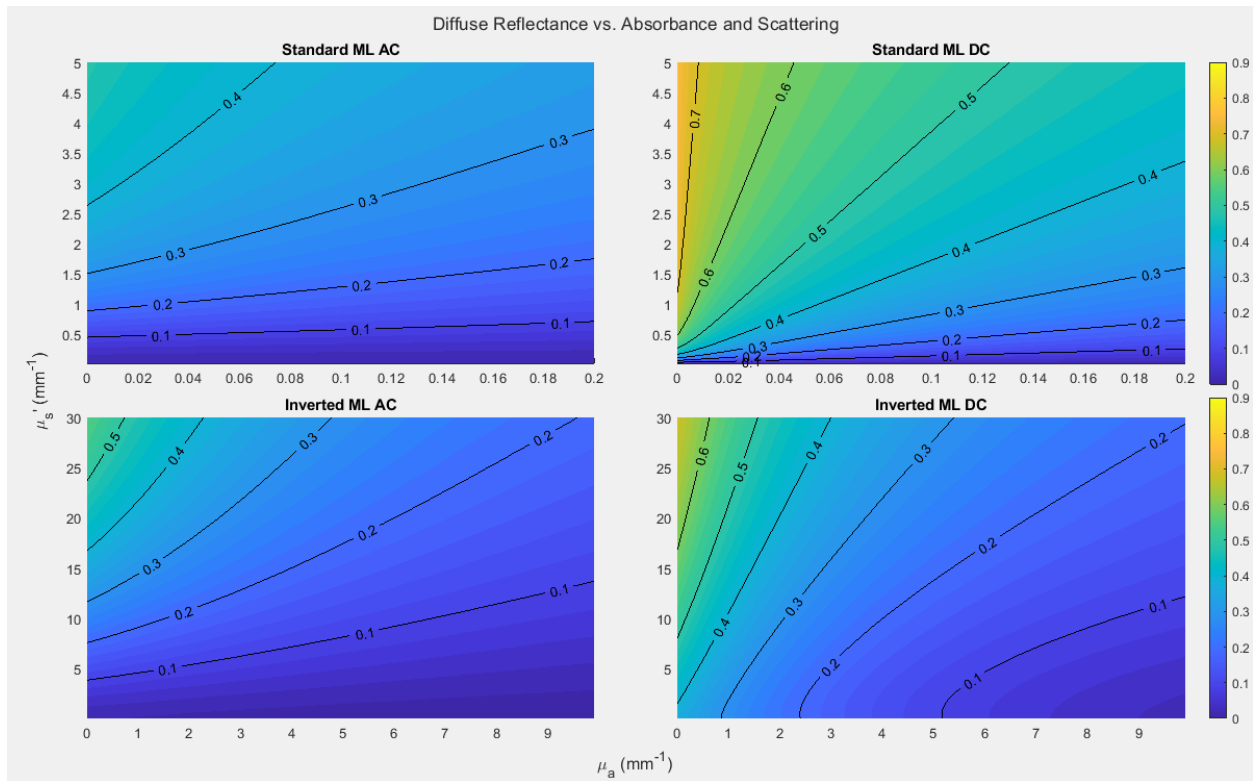
Figure 26: Comparison of LUT inversion algorithms based on a three-layer Fourier source approach with a light static simulated skin layer vs one with a dynamic simulated skin layer. (a) and (b) Optical properties versus AC Rd and DC Rd, respectively, for the MCX Gardner LUT. (c) and (d) Optical properties versus AC Rd and DC Rd, respectively, for the Fourier LUT.

To determine the relative accuracy when a LUT with an incorrect set of skin optical properties is used for skin testing, we performed a sensitivity analysis comparing LUTs generated with static or dynamic top layer optical properties. Figure 26 shows clearly how this shift impacts the LUTs behavior, as this is now testing for and focused on changing skin optical properties in a very shallow layer with significantly larger range of optical property values. Figure 27 does so similarly, with the altered shape demonstrating the qualitative difference between large shifts in a thin top layer's optical properties as compared to smaller shifts in a bottom layer of tissue.
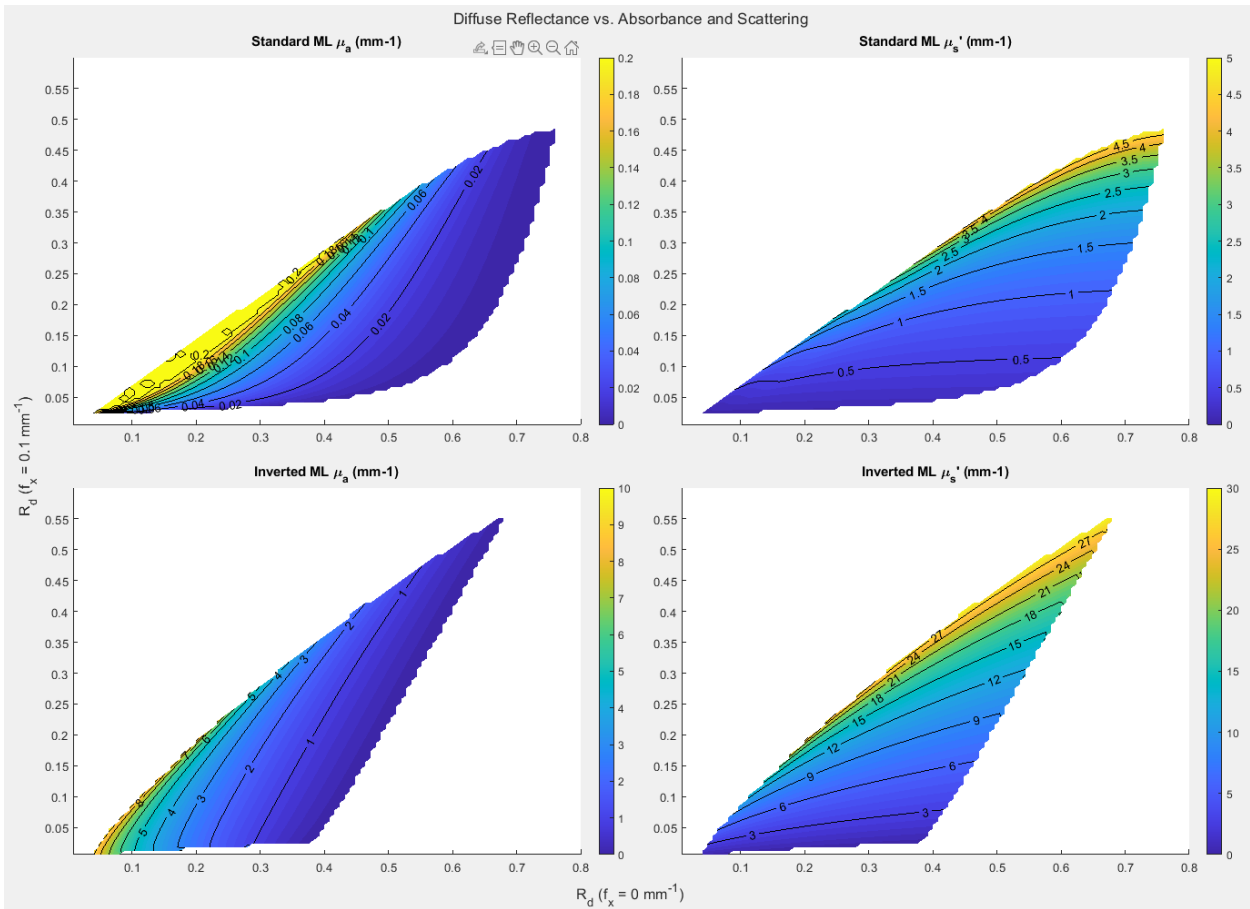
Figure 27: Comparison of optical property extractions using LUT inversion algorithms based on a three-layer MCX Fourier source with a light static simulated skin layer vs one with a dynamic simulated skin layer. (a) and (b) R_d values versus μ_a and μ_s', respectively, for the light skin Fourier LUT. (c) and (d) R_d values versus μ_a and μ_s', respectively, for the dark skin Fourier LUT, with relative axis scaling.

Figure 28 shows how the resulting error fits the patterns mostly as expected; absorption and scattering are largely independent of each other outside of edge cases; top layer absorption coefficient change has comparatively little impact on bottom layer scattering coefficient extraction, while changes in top layer scattering coefficient has a slightly greater but still low impact on bottom layer absorption coefficient extraction. Alterations in top layer scattering coefficients affect extracted scattering coefficients in the bottom layer, as expected, which can serve as useful confirmation but has little direct bearing as melanosome concentration should

not significantly influence scattering properties. However, absorption coefficient changes in the top layer have a very large impact on the extraction of absorption coefficients in the bottom layer over a range of values covering human skin complexion, very effectively demonstrating the inadequacy of any single LUT for use on all skin tones.

Figure 28: Comparison of absolute error in determined optical properties caused by inaccurate skin top layer optical property assumptions, using DOSI phantom properties as base of comparison. (a) error in extracted μ_a vs degree of inaccuracy in assumed top layer optical properties. (b) error in extracted μ_s' vs degree of inaccuracy in assumed top layer optical properties.

3.10 Conclusions

SFDI's medical utility is heavily dependent on the availability of accurate and applicable LUTs to reference, a lack of which has resulted in reduced health outcomes for marginalized patients. Taking full advantage of the potential of Monte Carlo modeling for simulations to

generate LUTs requires adapting to new and evolving computation abilities. MCX is able to make use of modern GPUs to vastly improve the speed of LUT generation, making more accurate simulation models practical as well as generating additional LUTs to account for a variety of skin types

We found that MCX can not only recreate the results of MCCL to a high degree of accuracy for Gardner method-based simulations, but produce the relevant LUTs up to two orders of magnitude faster thanks to GPU-based acceleration. This speed advantage is only partially mitigated when running Fourier-based simulations, which require more simulations to be performed per lookup table, but involve less post-processing of results. This speed advantage was most extreme for shorter anticipated pathlengths and higher scattering coefficients. The simulations with the greatest speed advantage were also those with the greatest overall time requirements. Together, this suggests that the processing of multiple scattering events is the primary bottleneck and that GPU-based acceleration can significantly ease the computational requirements for SFDI simulations,

The results of testing with adjusted photon counts show that while Gardner is less severely impacted by inadequate photon count simulations, Fourier is able to take advantage of increasing computing power for more directly analogous simulations with elevated potential accuracy. The voxel-based system of tissue simulation requires adaptation for multilayer testing, but these are surmountable problems with appropriate modifications to simulated optical properties in the relevant voxels for a given tissue layer. The alternate solution is significantly less plausible: memory problems become a serious issue at granular enough voxel densities to model the layer depths more precisely, as does the required increase in photon count to maintain sufficient area density to match distributions per surface voxel (for binning purposes), without providing a clear advantage based on our testing.

Fourier-based LUTs appear to be distinct from but comparable to Gardner LUTs, with the potential for more specificity in extracted optical properties based on returned diffuse

reflectance values. This holds true across homogenous LUTs, dark-skin based multilayer LUTs, and light-skin based multilayer LUTs. Similarly, both dark and light-skin based multilayer LUTs present in similar patterns, albeit at very different size scales, demonstrating the necessity of handling these skin types differently in SFDI.

Testing against real-world tissue phantom data show no serious disparities from expectations in multilayer tissue phantom testing (albeit with limited data), and show a serious accuracy advantage in homogenous tissue phantom testing in absorption coefficient extraction for Fourier LUTs over both MCX Gardner and MCCL Gardner LUTs.

Sensitivity analysis revealed a high level of error in extracted optical properties introduced by differences in LUT assumptions of top-layer optical properties from the true value of skin-layer optical properties in sample tissues. This was especially prevalent with regards to absorption coefficient error in the top layer propagating into error in extracted optical property values. Given melanin concentration differences in human populations primarily affect this parameter, it is particularly important to address. This clearly demonstrates the necessity of a range of LUTs to cover varied skin complexions for appropriate clinical use.

Overall, MCX Fourier patterned photon simulations show enormous promise in terms of fully utilizing modern computational resources for LUT generation, expanding the range of well-characterized skin types for more accurate use of SFDI. To take full advantage of this and ensure the correct LUTs are used for each patient, there's a need for clinically viable methods to efficiently and objectively approximate skin melanin concentrations to a close degree of specificity. Any follow up work should acquire a large range of high quality tissue phantoms of diverse skin tones to test against, with complete DOSI data, which we were unable to acquire during this testing. Easier generation will make it much more viable to generate and utilize a range of LUTs for varying skin tones to use with SFDI, a necessity given the clear and urgent need for better care of a diverse population.

REFERENCES

Alexandrakis, G., Farrell, T. J., & Patterson, M. S. (1998). Accuracy of the diffusion approximation in determining the optical properties of a two-layer turbid medium. In Applied Optics (Vol. 37, Issue 31, p. 7401). Optica Publishing Group. https://doi.org/10.1364/ao.37.007401

Angelo, J., Vargas, C. R., Lee, B. T., Bigio, I. J., & Giouxc, S. (2016, November). Ultrafast optical property map generation using lookup tables. *Journal of biomedical optics, 21*(11), 110501. doi:10.1117/1.JBO.21.11.110501

Bickler, P. E., Feiner, J. R., & Severinghaus, J. W. (2005). Effects of Skin Pigmentation on Pulse Oximeter Accuracy at Low Saturation. In Anesthesiology (Vol. 102, Issue 4, pp. 715–719). Ovid Technologies (Wolters Kluwer Health). https://doi.org/10.1097/00000542-200504000-00004

Bodenschatz, N., Brandes, A., Liemert, A., & Kienle, A. (2014, July). Sources of errors in spatial frequency domain imaging of scattering media. *Journal of biomedical optics, 19*(7), 071405. doi:10.1117/1.JBO.19.7.071405

Bodenschatz, N., Krauter, P., Liemert, A., Wiest, J., & Kienle, A. (2015, July). Model-based analysis on the influence of spatial frequency selection in spatial frequency domain imaging. *Applied Optics, 54*(22), 6725-6731. doi:10.1364/AO.54.006725

Burmeister, D. M., Ponticorvo, A., Yang, B., Becerra, S. C., Choi, B., Durkin, A. J., & Christy, R. J. (2015, September). Utility of spatial frequency domain imaging (SFDI) and laser speckle imaging (LSI) to non-invasively diagnose burn depth in a porcine model. *Burns : journal of the International Society for Burn Injuries, 41*(6), 1242-52. doi:10.1016/j.burns.2015.03.001

Busch, K., Soukoulis, C. M., & Economou, E. N. (1994). Transport and scattering mean free paths of classical waves. Physical review. B, Condensed matter, 50(1), 93–98. https://doi.org/10.1103/physrevb.50.93

Cuccia, D. J., Bevilacqua, F., Durkin, A. J., Ayers, F. R., & Tromberg, B. J. (2009, March-April). Quantitation and mapping of tissue optical properties using modulated imaging. *Journal of biomedical optics, 14*(2), 024012. doi:10.1117/1.3088140

Draghici, A. E., Potart, D., Hollmann, J. L., Pera, V., Fang, Q., DiMarzio, C. A., Andrew Taylor, J., Niedre, M. J., & Shefelbine, S. J. (2017). Near infrared spectroscopy for measuring changes in bone hemoglobin content after exercise in individuals with spinal cord injury. In Journal of Orthopaedic Research (Vol. 36, Issue 1, pp. 183–191). Wiley. https://doi.org/10.1002/jor.23622

Fang, Q., & Boas, D. A. (2009). Monte Carlo Simulation of Photon Migration in 3D Turbid Media Accelerated by Graphics Processing Units. In Optics Express (Vol. 17, Issue 22, p. 20178). Optica Publishing Group. https://doi.org/10.1364/oe.17.020178

Fawzy, A., Wu, T. D., Wang, K., Robinson, M. L., Farha, J., Bradke, A., Golden, S. H., Xu, Y., & Garibaldi, B. T. (2022). Racial and Ethnic Discrepancy in Pulse Oximetry and Delayed Identification of Treatment Eligibility Among Patients With COVID-19. In JAMA Internal Medicine (Vol. 182, Issue 7, p. 730). American Medical Association (AMA). https://doi.org/10.1001/jamainternmed.2022.1906

Gardner, A. R., & Venugopalan, V. (2011, June). Accurate and efficient Monte Carlo solutions to the radiative transport equation in the spatial frequency domain. *Optics letters, 36*(12), 2269-71. doi:10.1364/OL.36.002269

Gioux, S., Amaan, M., & Cuccia, D. J. (2019, June). Spatial frequency domain imaging in 2019: principles, applications, and perspectives. *Journal of biomedical optics, 24*(7), 1-18. doi:10.1117/1.JBO.24.7.071613

Haskell, R. C., Svaasand, L. O., Tsay, T. T., Feng, T. C., McAdams, M. S., & Tromberg, B. J. (1994). Boundary conditions for the diffusion equation in radiative transfer. Journal of the Optical Society of America. A, Optics, image science, and vision, 11(10), 2727–2741. https://doi.org/10.1364/josaa.11.002727

Hayakawa, C. K., Malenfant, L., Ranasinghesagara, J., Cuccia, D. J., Spanier, J., & Venugopalan, V. (2022). MCCL: an open-source software application for Monte Carlo simulations of radiative transport. In Journal of Biomedical Optics (Vol. 27, Issue 08). SPIE-Intl Soc Optical Eng. https://doi.org/10.1117/1.jbo.27.8.083005

Jacques, S. L. (2018) Assorted Spectra. Omlc.org. Retrieved July 19, 2024, from https://omlc.org/spectra/index.html

Jacques, S. L. (2022). History of Monte Carlo modeling of light transport in tissues using mcml.c. In Journal of Biomedical Optics (Vol. 27, Issue 08). SPIE-Intl Soc Optical Eng. https://doi.org/10.1117/1.jbo.27.8.083002

Jacques, S. L. (2023). Tutorial on Monte Carlo simulation of photon transport in biological tissues [Invited]. In Biomedical Optics Express (Vol. 14, Issue 2, p. 559). Optica Publishing Group. https://doi.org/10.1364/boe.477237

Khan, S. A., Bachchan, A., Devan, K., & Umasankari, K. (2021). Design methods and computer codes. In Physics of Nuclear Reactors (pp. 511–569). Elsevier. https://doi.org/10.1016/b978-0-12-822441-0.00012-1

Laughney, A. M., Krishnaswamy, V., Rice, T. B., Cuccia, D. J., Barth, R. J., Tromberg, B. J., . . . Wells, W. A. (2013, March). System analysis of spatial frequency domain imaging for quantitative mapping of surgically resected breast tissues. *Journal of biomedical optics, 18*(3), 036012. doi:10.1117/1.JBO.18.3.036012

Li, Y., Guo, M., Qian, X., Lin, W., Zheng, Y., Yu, K., . . . Xu, M. (2020, July). Single snapshot spatial frequency domain imaging for risk stratification of diabetes and diabetic foot. *Biomedical optics express, 11*(8), 4471-4483. doi:10.1364/BOE.394929

Ly, B. C., Dyer, E. B., Feig, J. L., Chien, A. L., & Bino, S. D. (2020, January). Research Techniques Made Simple: Cutaneous Colorimetry: A Reliable Technique for Objective Skin Color Measurement. *Journal of Investigative Dermatology, 140*(1), 3-12. doi:10.1016/j.jid.2019.11.003

Mazhar, A., Dell, S., Cuccia, D. J., Gioux, S., Durkin, A. J., Frangioni, J. V., & Tromberga, B. J. (2010, November-December). Wavelength optimization for rapid chromophore mapping using spatial frequency domain imaging. *Journal of biomedical optics, 15*(6), 061716. doi:10.1117/1.3523373

Mazhar, A., Saggese, S., Pollins, A. C., Cardwell, N. L., Nanney, L., & Cuccia, D. J. (2014, August). Noncontact imaging of burn depth and extent in a porcine model using spatial

frequency domain imaging. *Journal of biomedical optics, 19*(8), 086019. doi:10.1117/1.JBO.19.8.086019

Meglinski, I. V., & Matcher, S. J. (2002, November). Quantitative assessment of skin layers absorption and skin reflectance spectra simulation in the visible and near-infrared spectral regions. *Physiological measurement, 23*(4), 741-53. doi:10.1088/0967-3334/23/4/312

Nadeau, K. P., Durkin, A. J., & Tromberg, a. B. (2014, May). Advanced demodulation technique for the extraction of tissue optical properties and structural orientation contrast in the spatial frequency domain. *Journal of biomedical optics, 19*(5), 056013. doi:10.1117/1.JBO.19.5.056013

Nitzan, M., Romem, A., & Koppel, R. (2014). Pulse oximetry: fundamentals and technology update. In Medical Devices: Evidence and Research (p. 231). Informa UK Limited. https://doi.org/10.2147/mder.s47319

Ntziachristos, V. (2010). Going deeper than microscopy: the optical imaging frontier in biology. In Nature Methods (Vol. 7, Issue 8, pp. 603–614). Springer Science and Business Media LLC. https://doi.org/10.1038/nmeth.1483

Phan, T., Rowland, R., Ponticorvo, A., Le, B. C., Wilson, R. H., Sharif, S. A., . . . Durkina, A. J. (2021, February). Characterizing reduced scattering coefficient of normal human skin across different anatomic locations and Fitzpatrick skin types using spatial frequency domain imaging. *Journal of biomedical optics, 26*(2), 026001. doi:10.1117/1.JBO.26.2.026001

Pilvar, A., Mehendale, A. M., Karrobi, K., El-Adili, F., Bujor, A., & Roblyer, D. (2023). Spatial frequency domain imaging for the assessment of scleroderma skin involvement. Biomedical optics express, 14(6), 2955–2968. https://doi.org/10.1364/BOE.489609

Ragunathan, R. (2021, Jan 15) Fwd: Fwd: MCX simulation of SFDI. Google Groups. Retrieved July 19, 2024, from https://groups.google.com/g/mcx-users/c/nr_ZB3HE8fI/m/j0IBfStgBQAJ?hl=en

Reble, C., Gersonde, I., Lieber, C. A., & Helfmann, J. (2011, February). Influence of tissue absorption and scattering on the depth dependent sensitivity of Raman fiber probes investigated by Monte Carlo simulations. *Biomedical optics express, 2*(3), 520-533. doi:10.1364/BOE.2.000520

Rohrbach, D. J., Muffoletto, D., Huihui, J., Saager, R., Keymel, K., Paquette, A., . . . Sunar, U. (2014, February). Preoperative Mapping of Nonmelanoma Skin Cancer Using Spatial Frequency Domain and Ultrasound Imaging. *Academic radiology, 21*(2), 263-270. doi:10.1016/j.acra.2013.11.013

Sjoding, M. W., Dickson, R. P., Iwashyna, T. J., Gay, S. E., & Valley, T. S. (2020). Racial Bias in Pulse Oximetry Measurement. The New England journal of medicine, 383(25), 2477–2478. https://doi.org/10.1056/NEJMc2029240

Smith, J. D. (2002). W.E.B. Du Bois, Felix von Luschan, and Racial Reform at the Fin de Siècle. Amerikastudien / American Studies, 47(1), 23–38. http://www.jstor.org/stable/41157700

Sudat, S. E. K., Wesson, P., Rhoads, K. F., Brown, S., Aboelata, N., Pressman, A. R., Mani, A., & Azar, K. M. J. (2023). Racial Disparities in Pulse Oximeter Device Inaccuracy and

Estimated Clinical Impact on COVID-19 Treatment Course. American journal of epidemiology, 192(5), 703–713. https://doi.org/10.1093/aje/kwac164

Tabassum, S., Pera, V., Greening, G., Muldoon, T. J., & Roblyer, D. (2018, July). Two-layer inverse model for improved longitudinal preclinical tumor imaging in the spatial frequency domain. *Journal of biomedical optics, 23*(7), 1-12. doi:10.1117/1.JBO.23.7.076011

Thinh Phan, R. R. (2022, March). Quantifying the confounding effect of pigmentation on measured skin tissue optical properties: a comparison of colorimetry with spatial frequency domain imaging. *Journal of biomedical optics, 27*(3), 036002. doi:10.1117/1.JBO.27.3.036002

Weinkauf, C., Mazhar, A., Vaishnav, K., Hamadani, A. A., Cuccia, D. J., & Armstrong, D. G. (2019, February). Near-instant noninvasive optical imaging of tissue perfusion for vascular assessment. *Journal of vascular surgery, 69*(2), 555-562. doi:10.1016/j.jvs.2018.06.202

Yafi, A., Muakkassa, F. K., Pasupneti, T., Fulton, J., Cuccia, D. J., Mazhar, A., Blasiole, K. N., & Mostow, E. N. (2017). Quantitative skin assessment using spatial frequency domain imaging (SFDI) in patients with or at high risk for pressure ulcers. Lasers in surgery and medicine, 49(9), 827–834. https://doi.org/10.1002/lsm.22692

Yan, S., Yao, R., Intes, X., & Fang, Q. (2020, May). Accelerating Monte Carlo modeling of structured-light based diffuse optical imaging via "photon sharing". *Optics letters, 45*(10), 2842-2845. doi:10.1364/OL.390618

APPENDIX

Computer specifications used for bulk of simulations:

Processor: Intel(R) Core(TM) i5-10400 CPU @ 2.90GHz   2.90 GHz

RAM: 16.0 GB

Windows 10

MATLAB R2021a

GPU: NVIDIA GeForce GTX 1660

PC used to run e9 photon count Fourier source simulations:

Processor: Processor Intel(R) Core(TM) i7-8700 CPU @ 3.20GHz, 3192 Mhz, 6 Core(s), 12 Logical Processor(s)

RAM: 32 GB

Windows 10 Pro

MATLAB R2021a

GPU: NVIDIA Quadro RTX 4000

MCCL Parameters

1e7 photons

MersenneTwister RNG type

Continuous Absorption Weighting (not Discrete)

HenyeyGreenstein phase function type

pMCDiffuseReflectance database

No russian roulette

Directional point source at 0,0,0, direction vector 0,0,1

Mus 1e-10 scattering for infinite layers on either side

200mm thick tissue

L* values

    <"Mua": 0.0198,

    "Mus": 6.8276,

    "G": 0.71,

    "N": 1.33,

    "Musp": 1.98>

51 fx from 0 to 0.5mm^-1

ROfFx detector

Scripts and Coding Files

All MATLAB scripts and code used are available in the following git repository:

https://github.com/DaemonDikeman/MCXFourier2024/

We used LUT_Graphs for early LUT testing and verification, and Multilayer_Models_Plot for early comparisons of multilayered LUTs during testing.

In order to acquire the visualization plots, we used a number of scripts: to generate contour lined heat map comparisons, we used [Contours (list)]; to generate cross-method line plot comparisons, we used Triple_Comparison_Plot; to generate line plot comparisons of performance with variable photon counts, we used LStar_Combined Plot.

To generate the data used for the line plot comparisons, we used Two_Layer_LUT_DRef_Comparison, Multi_Layer_Gardner_Dref_Comp, and Single_Layer_Homogenous_Dref_Comp.

LUTs were generated using a variety of scripts: SFDI_MCX_Start_Traj was used for early prototyping; SFDI_MCX_Fourier_LUT_Gen.m for both homogenous and multilayer Fourier LUTs; SFDI_MCX_Fourier_LUT_Gen_Flipped.m for sensitivity analysis; Single_Layer_Homogenous_LUT_Generation_mba for homogenous Gardner LUTs; and Two_Layer_LUT_Generation_MCX for generating Gardner LUTs.

We used a modified version of Analysis_Workflow as part of our practical tests of performance on real tissue phantoms.

Single_photon_Pencil_Source_Display

ChromophoreSpectraPlot - credit to camorbit code by FINNSTAR7
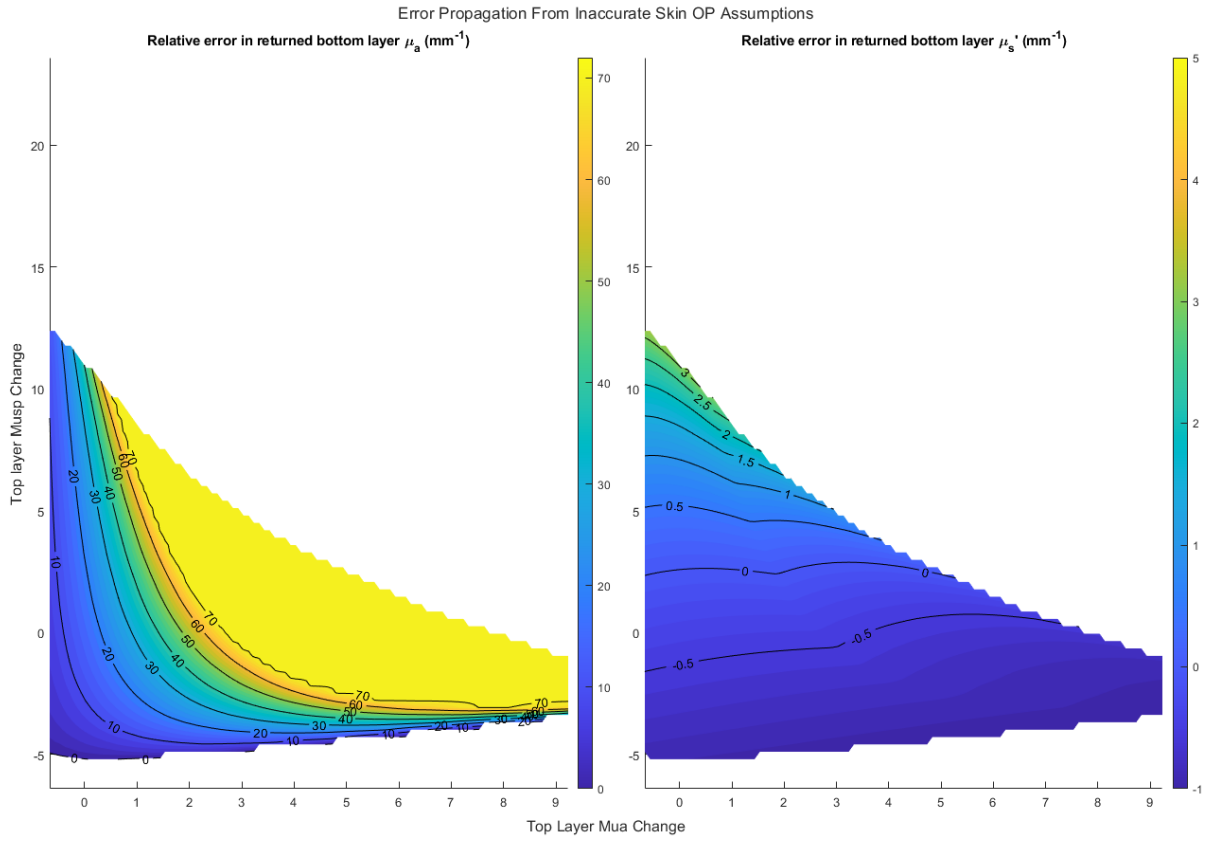
Figure A.1. Relative Error in OP Extraction vs Skin Layer OP Divergence
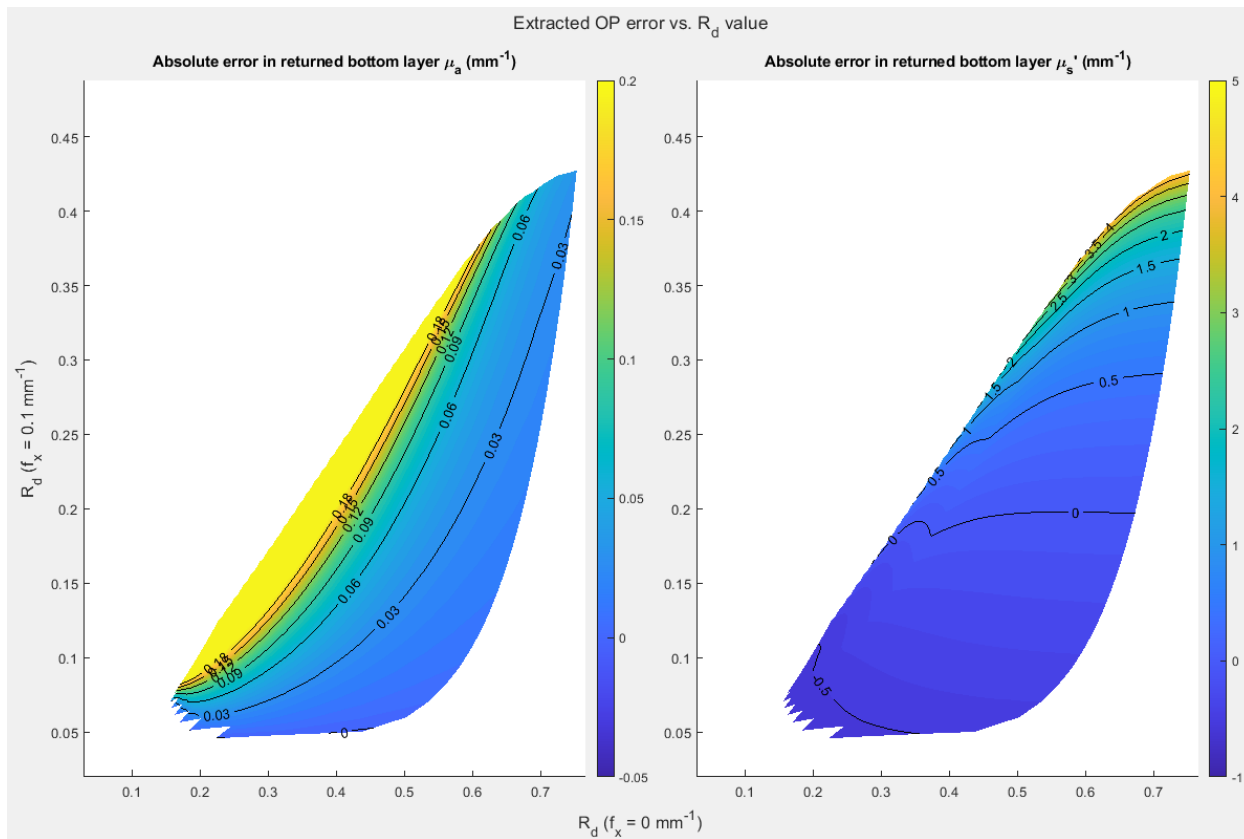
Figure A.2. Error in OP Extraction vs R_d

BIOGRAPHY OF THE AUTHOR

Daemon Dikeman was born in Clarksburg, West Virginia on December 12th, 1997. He was raised in Oregon and graduated from Canby High School in 2016. He attended Oregon State University and graduated in 2020 with a Bachelors degree in Biochemistry & Molecular Biology with a specialization in Advanced Molecular Biology. He moved to Maine in 2020 to pursue his graduate career in Biomedical Science and Engineering at the University of Maine, transitioning from Biomedical Science to Biomedical Engineering in 2021. He is a candidate for the Master of Science degree in Biomedical Engineering from the University of Maine in August 2024.